AIMS Mathematics, 11(10): 34730–34762.
DOI: 10.3934/math.20261353
Received: 25 August 2026
Revised: 27 September 2026
Accepted: 09 October 2026
Published: 26 October 2026

https://www.aimspress.com/journal/Math

Research article

Mathematical and machine learning analysis of MHD ternary hybrid nanofluid flow through a porous-baffled corrugated channel

Talal Ali Alzahrani* and Saleh Mousa Alzahrani

Department of Mathematics, University College in Al-Qunfudhah, Umm Al-Qura University, Al-Qunfudhah, Saudi Arabia

* **Correspondence:** Email: tazahrani@uqu.edu.sa.

Abstract: Efficient thermal management in compact engineering systems requires enhanced heat transfer with minimal hydraulic penalties. This study investigates the magnetohydrodynamics (MHD) of forced convection of a Cu–CuO–Al_2O_3/water ternary hybrid nanofluid in a corrugated channel equipped with porous baffles. Unlike previous studies primarily using impermeable baffles, the present work combines corrugated heated walls, permeability-controlled porous baffles, ternary hybrid nanofluid transport, and artificial neural network (ANN)-based surrogate modeling within a unified framework. The governing equations are discretized and solved using the finite element method (FEM), where the clear fluid region is modeled using the Navier–Stokes equations and the porous baffle's region is modeled using the Darcy–Brinkman–Forchheimer formulation under local thermal equilibrium (LTE). The effects of the Reynolds number (Re), Darcy number (Da), Hartmann number (Ha), and nanoparticle volume fraction (ϕ) are analyzed in terms of streamlines, isotherms' contours, Nusselt numbers, pressure drop, and the thermo-hydraulic performance index. The results show that replacing solid baffles with porous baffles increases the mean Nusselt number by approximately 5.55% while reducing the pressure drop by 13.22%. Furthermore, increasing the Da from 10^{-6} to 10^{-2} enhance the mean Nusselt number by approximately 13.14% and decrease the pressure drop by 9.36%, demonstrating the importance of permeability-controlled flow penetration. The performance index remains above unity, conforming a favorable balance between thermal enhancement and hydraulic resistance. To complement the mathematical simulations, feedforward ANNs using hyperbolic tangent sigmoid function and Levenberg–Marquart taring are developed to predict the U-velocity, V-velocity, temperature, and Nusselt number from the FEM-generated datasets. Regression, error, residual, and FEM-ANN comparisons demonstrate strong predictive agreement, conforming the capability of the ANN models to reproduce the nonlinear

thermo-hydrodynamic responses. The combined FEM-ANN framework provides an effective approach for analyzing and predicting coupled MHD transport in porous flow systems.

Keywords: machine learning; magnetohydrodynamics; porous baffles; ternary hybrid nanofluid; finite element method; Darcy–Brinkman–Forchheimer model
Mathematics Subject Classification: 76A05, 76S05, 80A20

1. Introduction

Effective thermal management has become a major requirement in modern engineering systems because of the rapid increase in power density, device miniaturization, and the growing demand for compact and high-efficiency thermal systems. Applications such as electronic cooling, compact heat exchangers, battery thermal management, solar thermal collectors, microchannel heat sinks, and energy conversion devices require efficient heat removal with minimum pumping power. Conventional smooth channel cooling systems often fail to provide sufficient thermal performance because of their limited heat transfer area, weak fluid mixing, and the formation of stable thermal boundary layers near heated walls. Therefore, considerable research attention has been devoted to passive heat transfer enhancement techniques, including extended surfaces, corrugated walls, baffles, porous media, and advanced working fluids.

Extended surfaces, and the related obstacles, are among the best-known passive enhancement options, because they raise the available heat transfer area and, at the same time, make thermal contact better between the heated boundary and the fluid flow. Pishkar and Ghasemi [1] reported that when fins are used inside a horizontal channel, the cooling improves even under mixed convection, and they also explained that the spacing between those fins matters greatly for heat removal further downstream. Khentoul and Bessaïh [2] carried out a numerical study of entropy generation in a horizontal finned channel with a Cu–Al_2O_3/water hybrid nanofluid (HNF), and they observed that when fin height increases, heat transfer goes up; however, this trend also brings changes in irreversibility and in the hydraulic resistance as well. Taken together, these papers indicate that internal inserts can indeed boost the thermal response, but the arrangement and the geometry need to be tuned carefully, so the pressure losses do not become too high.

Porous media have also received much attention in thermal engineering because they give a large surface area, help with flow redistribution, and strongly interact between the fluid and the solid matrix. Porous structures may disrupt the thermal boundary layer somewhat but, at the same time, they can boost the effective heat transfer area, even while permitting partial flow to enter into the medium, in a gentle manner. Kim et al. [3] worked on flow resistance and heat transport for porous fins inside plate-fin heat exchangers and they showed that porous fins can really improve the heat removal capability of compact heat exchangers. Arjun and Rakesh [4] looked at porous pin fins with nanofluid (NF) flow in rectangular corrugated minichannels, and they said that the porous pin fin arrangements offered better heat transfer than the usual solid fins. Deshamukhya et al. [5] reviewed more recent progress on porous fins, and they concluded that porous fins typically outperform solid fins in both forced convection and natural convection, yet the associated nonlinear transport equations need careful analytical and numerical handling.

The use of NFs shows up as another key development for heat transfer enhancement. Choi and

Eastman [6] first came up with the idea of NFs by placing nanoscale solid particles inside base fluids, mainly so the thermal conductivity could more or less be upgraded. Since that time, many works have pointed out that a nanoparticle suspension can boost the heat transport ability of the base liquid. Still, mono-NFs sometimes run into stability concerns, and they may show higher viscosity as well, which then can raise pumping power. Smrity and Yin [7] used HNF modeling and validation methods, and they noted that HNFs are able to deliver improved thermal conductivity plus more sensible tuning of the thermophysical properties when compared with mono-NFs. Rashid et al. [8] then looked at NF usage in plate heat exchangers, and their results suggested that both NFs and HNFs improve heat transfer performance, even if the impact of pressure drop is still a big design constraint. Rashid et al. [9] also reviewed free convection occurring in trapezoidal enclosures that are filled with NF and HNF, and they stressed that the nanoparticles' nature, cavity shape, and the specified wall temperature conditions strongly steer the overall heat transfer behavior. Recent investigations have extended HNF research toward MHD thermal transport and machine learning-assisted prediction. Hafeez et al. [10] examined radiative MHD HNF flow with melting effects, Khalid et al. [11] combined computational fluid dynamics (CFD) with artificial neural networks (ANNs) for nano-enhanced thermal energy storage prediction, while Jalili et al. [12] investigated the effects of magnetic fields on HNF transport between parallel sheets. Mahmood et al. [13] numerically investigated non-Newtonian fluid flow in a channel-driven cavity containing a square obstacle and demonstrate the influence geometrical parameters of the flow characteristics. Bilal et al. [14] examined the coupled heat and mass transfer of a power-law fluid in a lid-driven corrugated chamber using the finite element method (FEM).

Ternary HNFs (THNFs) are more advanced class of working fluids as compared with NFs and HNFs. THNFs are composed of three distinct nanoparticle species in one base fluid which can be used to adjust the thermal, rheological, and stability properties more effectively. Adun et al. [15] investigated THNFs and determined that the thermal conductivity and heat transport performance of THNFs could be better than that of NFs and HNFs. Alqarni et al. [16] numerically showed the enhancement of heat transfer for THNF flow when it flows in convergent and divergent channels, due to the better thermophysical properties of the ternary NF. Rabby et al. [17] summarized recent advancements in THNFs and mention significant enhancements of heat conduction capability, heat transport coefficient, and thermo-hydraulic performance. Nayak et al. [18] reviewed the stability and heat transfer applications of THNF and demonstrated that the combination of particles, the preparation methods, and the control of the stability of the NFs are crucial for any practical applications. Pandian and Boobalan [19] also noted that the use of THNF is highly promising for several applications, such as electronics cooling, renewable energy applications, automotive thermal management, and advanced heat transport applications.

Studies have reported that porous media and NFs are a powerful hybrid enhancement strategy. Khalaf et al. [20] surveyed the enhancement of heat transfer through porous media, NFs and obstacles. They reported that the combination of the abovementioned passive techniques can yield significant increases in the thermal performance. Jarray et al. [21] studied the forced convection of an Ag–MgO/water HNF in a porous horizontal corrugated channel and found that the thermal enhancement of HNF was better than that of NF in a large range of Richardson and Darcy (Da) numbers. Alsabery and Abosinee [22] investigated the heat transfer distribution and flow structure for forced convection of a NF in a partly filled porous straight channel, in which they found that the flow structure and heat transfer distribution were strongly affected by the porous section. Rahomey

et al. [23] discussed the laminar forced convection of NF through various channels and showed the potential of a porous media configuration for enhancing thermal behavior. Asbagh et al. [24] reviewed the enhancement of heat transfer in multiphase flow systems consisting of NFs, microchannels, and porous media and found that hybrid techniques can give improved thermo-hydraulic performance as compared with single techniques. Recent studies have increasingly combined advanced NF modeling with artificial intelligence (AI) techniques. Min et al. [25] investigated AI-assisted heat transfer analysis of Williamson NFs over a vertically stretching sheet, Arian et al. [26] used nonlinear autoregressive network with exogenous inputs denoted by (NARX) neural networks to model acoustic-driven bubble dynamics in Williamson fluids, while Zulifiqar et al. [27] numerically examined coupled heat and mass transfer in bioconvective Oldroyd-B NF flow over a porous Riga surface.

Because of the consideration of porous media, NFs, magnetic fields, and complex geometry, the governing equations for these types of coupled flow and heat transfer systems are highly nonlinear, so numerical modeling is essential to analyze these systems. The FEM is popular, since it can be applied to an irregular geometry, a multidomain configuration, and a coupled transport equation. Sobamowo [28] conducted a FEM investigation of the thermal behavior of a moving porous fin by considering the temperature-dependent heat conduction capability and internal heat generation. Ahmed et al. [29] performed a study of the flow and thermal field of NFs in inclined U-shaped enclosures using FEM simulation and studied the effects of multiple heat-generating permeable baffles. Rashidi et al. [30] used the Darcy–Brinkman–Forchheimer model to numerically investigate forced convective flow over a square diamond-shaped porous cylinder. Their results revealed that increasing the Da reduced the drag force and delayed the onset of flow separation. The studies above are validations of the use of FEM for complex porous media and NF heat transfer problems.

Porous obstacles are especially appealing for channel flow applications, as they offer the mixing of solid baffles and the flow penetration of porous media. In a rectangular channel, Ko and Anand [31] studied the use of porous obstacles for thermal enhancement and found that porous obstacle can offer substantial thermal enhancement through encouraging fluid mixing and heat dispersion within the porous matrix. Santos and de Lemos [32] examined the influence of solid and porous baffles on the thermo-hydraulic performance of a parallel-plate channel and found that porous baffles can alleviate the large hydraulic penalty which is caused by impermeable solid baffles. These studies show that substituting solid barriers with porous baffles can be a successful way to thermal enhancement while reducing the hydraulic loss.

The control of electrically conducting fluid flows is also an important mechanism of MHD. The induced Lorentz force changes the velocity field and affects the thermal boundary layer when applied in the presence of MHD flow conditions. In the case of NF and THNF systems, the modified electrical and thermal properties of the working fluid can be acted upon by the magnetic field. The Hartmann number (Ha) is thus a significant parameter for controlling the flow damping, thermal transport and pressure drop. Lorentz force, Darcy resistance, Forchheimer drag, and nanoparticle-enhanced thermal conductivity all affect the flow in a porous-baffled corrugated channel. This results in a complicated thermo-hydraulic response which needs thorough numerical modeling. Recent investigations have increasingly focused on the combined effects of the magnetic field, porous media, advanced NFs, and data-driven modeling in thermal transport systems. Hussein et al [33] investigated the heat transfer and flow characteristics of THNF over a permeable surface under a magnetic field. Kundu et al. [34] combined FEM with ANN and response surface modeling to

analyze magnetically influenced Cu–CuO–Al_2O_3/water THNFs' convection. Haider et al. [35] used ANN modeling to investigate the heat and mass transfer of magnetically controlled THNFs through porous media. These studies demonstrate growing interest in integrating advanced working fluids, porous structures, magnetic control, and data-driven modeling; however, their combined application to forced convection in a corrugated channels containing permeable baffles remains comparatively limited.

The literature above demonstrates substantial progress in finned and corrugated channels, porous media, porous baffles, NFs and HNFs, and MHD-assisted thermal transport. However, these enhancement strategies have predominantly been investigated individually or in conventional channel configurations. In corrugated channels, impermeable obstacles are commonly used to intensify fluid mixing and heat transfer, but the resulting enhancement is often accompanied by an increased pressure-drop penalty. Although porous baffles offer the possibility of reducing the flow resistance through permeability-controlled penetration, their combined use with THNFs under an imposed magnetic field in corrugated channels remains insufficiently explored. In particular, the coupled effects of baffle permeability, porosity, magnetic damping, and nanoparticle loading on the heat transfer–pressure drop trade-off require systematic investigation. Furthermore, efficient data-driven representation of the spatial thermo-hydrodynamic responses of such systems remains limited.

To address the identified research gap, the present study develops a combined mathematical, numerical, and machine learning framework for investigating the thermo-hydraulic characteristics of MHD THNF flow through a corrugated channel equipped with porous baffles. The upper and lower corrugated walls are maintained at a uniform hot temperature T_h, whereas the porous baffles are kept adiabatic; they are used as passive flow-control elements but not as additional heat sources. The incompressible Navier–Stokes equations and energy equation with the MHD body force term are used for the clear fluid region, and the Darcy–Brinkman–Forchheimer approach is used for the porous baffle regions. The main purpose of the present work is to investigate the Reynolds number (Re), Ha, the volume fraction of ternary nanoparticles, Darcy number (Da), and porosity effects on the streamlines, isotherms, average Nusselt number, pressure drop, and thermo-hydraulic performance index.

The principal originality of the present work lies in integrating permeability-controlled porous baffles, corrugated isothermal walls, THNF transport, and magnetic damping within a unified thermo-hydraulic framework. Unlike conventional impermeable baffles, the porous configuration permits fluid penetration through the obstacles, providing an additional mechanism for controlling the enhancement of heat transfer and the hydraulic resistance. The study further integrates FEM-generated data with a feedforward ANN using the spatial coordinates and the governing physical parameters as inputs to reproduce the U-velocity, V-velocity, temperature, and local Nusselt number responses. The resulting FEM-ANN framework therefore provides both a physical-based assessment of the porous baffle configuration and an efficient data-driven surrogate for representing its nonlinear thermo-hydrodynamics behavior within the investigated parameter domain.

2. Mathematical modeling

2.1. Problem description

The present study considered a two-dimensional corrugated channel filled with THNF in the presence of a transverse magnetic field (B_0). The proposed geometry is developed as an extension of the wavy obstacle corrugated channel investigated in the reference study [36], in which impermeable solid obstacles were positioned at different locations to enhance MHD NF heat transfer. In the present configuration, the solid obstacles are replaced by permeable porous baffles arranged along the bottom-center line (BCL), allowing partial flow penetration through the baffle regions while maintaining effective thermal mixing and reducing the pressure drop penalty caused by complete flow obstruction. The channel consists of a straight inlet section of length $3L$ to ensure fully developed flow, a central wavy section of length $15L$ and a straight outlet section of length $5L$, giving a total length of $23L$. The total channel height is $2L$. The top and bottom walls of the central corrugated section are maintained at the uniform hot temperature T_h. Six square porous baffles of size 0.5L × 0.5L are placed inside the wavy section according to the BCL configuration, as shown in Figure 1. The porous baffles are assumed to be adiabatic and act only as passive flow control elements. The left inlet serves as the entry point for a cold THNF, which flows into the channel at a uniform velocity and a temperature of T_c.

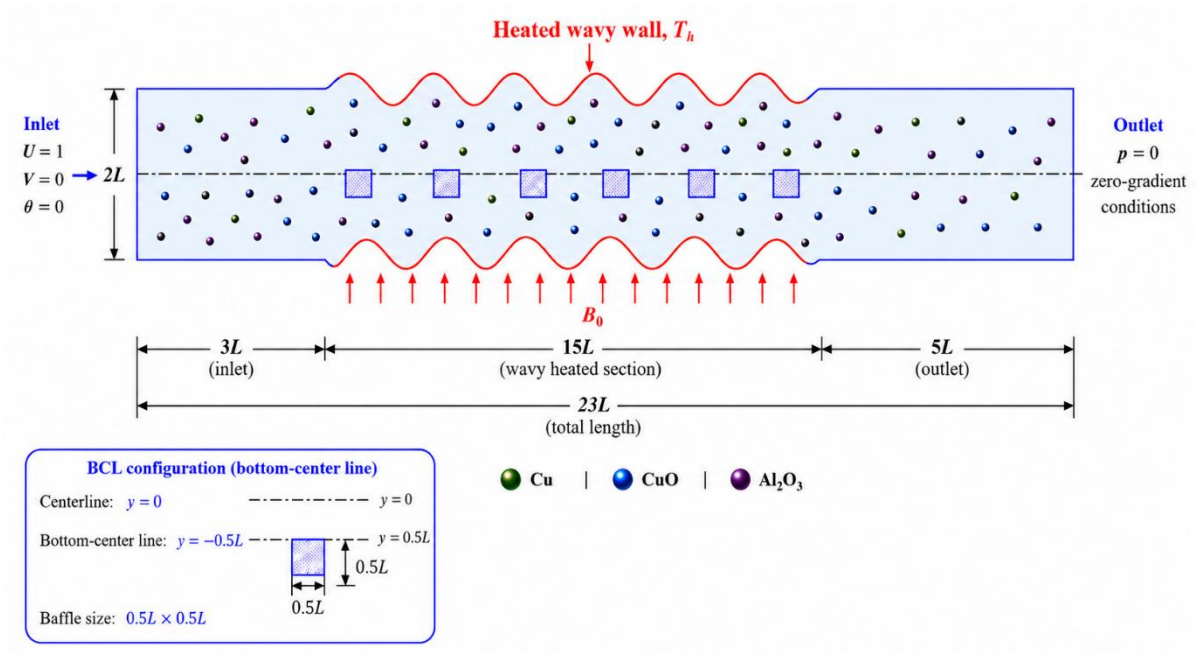


Figure 1. Schematic of a corrugated channel with porous baffles arranged in the BCL configuration.

2.2. Governing equations

The present study considers a two-dimensional, steady, laminar, and incompressible flow of a THNF through a corrugated channel fitted with porous baffles. To accurately capture the transport phenomena in the computational domain, separate mathematical formulations are adopted for the

clear fluid and porous regions. The fluid motion in the open channel is governed by the incompressible Navier–Stokes equations, whereas the flow inside the porous baffles is represented by the Darcy–Brinkman–Forchheimer model, which incorporates viscous diffusion as well as inertial resistance associated with porous media. The porous baffles are assumed to possess homogeneous and isotropic structural characteristics, ensuring uniform permeability throughout the porous domain. In addition, the thermophysical properties of the THNF are considered to be temperature-independent, except for the effective properties that are modified according to the nanoparticles' volume fraction. Since the thermal interaction between the porous matrix and the working fluid is sufficiently strong, the local thermal equilibrium (LTE) assumption is adopted, allowing both phases to share an identical temperature field. Furthermore, radiation, viscous dissipation, and compressibility effects are neglected to simplify the mathematical model without compromising the accuracy of the present analysis under the specified operating conditions. Based on these assumptions, the governing equations describing the conservation of mass, momentum, and energy are formulated as follows [30].

2.2.1. Clear fluid region

$$\frac{\partial u^{(f)}}{\partial x} + \frac{\partial v^{(f)}}{\partial y} = 0. \tag{1}$$

$$\rho_{thnf}\left(u^{(f)}\frac{\partial u^{(f)}}{\partial x} + v^{(f)}\frac{\partial u^{(f)}}{\partial y}\right) = -\frac{\partial p^{(f)}}{\partial x} + \mu_{thnf}\left(\frac{\partial^2 u^{(f)}}{\partial x^2} + \frac{\partial^2 u^{(f)}}{\partial y^2}\right) - \sigma_{thnf}B_0^2 u^{(f)}. \tag{2}$$

$$\rho_{thnf}\left(u^{(f)}\frac{\partial v^{(f)}}{\partial x} + v^{(f)}\frac{\partial v^{(f)}}{\partial y}\right) = -\frac{\partial p^{(f)}}{\partial y} + \mu_{thnf}\left(\frac{\partial^2 v^{(f)}}{\partial x^2} + \frac{\partial^2 v^{(f)}}{\partial y^2}\right). \tag{3}$$

$$\left(u^{(f)}\frac{\partial T_f}{\partial x} + v^{(f)}\frac{\partial T^{(f)}}{\partial y}\right) = \alpha_{thnf}\left(\frac{\partial^2 T^{(f)}}{\partial x^2} + \frac{\partial^2 T^{(f)}}{\partial y^2}\right). \tag{4}$$

Here, $u^{(f)}$ and $v^{(f)}$are the velocity components in the clear fluid region, $p^{(f)}$ is the pressure, $T^{(f)}$ is the temperature, ρ_{thnf} is the density, μ_{thnf} is the dynamic viscosity, k_{thnf} is the thermal conductivity, and $\left(\rho C_p\right)_{thnf}$ is the heat capacity product of the THNF.

2.2.2. Porous fin region

In the porous fin region, the fluid motion is governed by the Darcy–Brinkman–Forchheimer model. The Brinkman term accounts for viscous diffusion inside the porous medium, the Darcy term represents linear porous resistance, and the Forchheimer term represents nonlinear inertial resistance. The dimensional conservation equations are written as follows [30]:

$$\frac{\partial u^{(p)}}{\partial x} + \frac{\partial v^{(p)}}{\partial y} = 0. \tag{5}$$

$$\frac{\rho_{thnf}}{\varepsilon^2}\left(u^{(p)}\frac{\partial u^{(p)}}{\partial x}+v^{(p)}\frac{\partial u^{(p)}}{\partial y}\right)=-\frac{\partial p^{(p)}}{\partial x}+\frac{\mu_{thnf}}{\varepsilon}\left(\frac{\partial^2 u^{(p)}}{\partial x^2}+\frac{\partial^2 u^{(p)}}{\partial y^2}\right)-\frac{\mu_{thnf}}{K_f}u^{(p)}-\frac{\rho_{thnf}\,C_F}{\sqrt{K_f}}\left(\sqrt{{u^{(p)}}^2+{v^{(p)}}^2}\right)u^{(p)}-\sigma_{thnf}B_0^2u^{(p)}. \tag{6}$$

$$\frac{\rho_{thnf}}{\varepsilon^2}\left(u^{(p)}\frac{\partial v^{(p)}}{\partial x}+v^{(p)}\frac{\partial v^{(p)}}{\partial y}\right)=-\frac{\partial p^{(p)}}{\partial y}+\frac{\mu_{thnf}}{\varepsilon}\left(\frac{\partial^2 v^{(p)}}{\partial x^2}+\frac{\partial^2 v^{(p)}}{\partial y^2}\right)-\frac{\mu_{thnf}}{K_f}v^{(p)}-\frac{\rho_{thnf}\,C_F}{\sqrt{K_f}}\left(\sqrt{{u^{(p)}}^2+{v^{(p)}}^2}\right)v^{(p)}. \tag{7}$$

For heat transfer in the porous baffle region, the LTE assumption is adopted, under which the fluid saturating the porous medium and the solid matrix are assumed to share the same local temperature [37]. This approach permits the thermal transport in the two phases to be represented by a single volume-averaged energy equation using effective thermophysical properties. Thus, we have

$$T^{(f)}=T^{(s)}=T^{(p)}.$$

The effective energy equation is written as

$$\left(\rho C_p\right)_{eff}\left(u_D^{(p)}\frac{\partial T^{(p)}}{\partial x}+v_D^{(p)}\frac{\partial T^{(p)}}{\partial y}\right)=k_{eff}\left(\frac{\partial^2 T^{(p)}}{\partial x^2}+\frac{\partial^2 T^{(p)}}{\partial y^2}\right). \tag{8}$$

The effective thermal conductivity and heat capacity product of the porous region are evaluated as

$$k_{eff}=\varepsilon k_{thnf}+(1-\varepsilon)k_s. \tag{9}$$

$$\left(\rho C_p\right)_{eff}=\varepsilon\left(\rho C_p\right)_{thnf}+(1-\varepsilon)\left(\rho C_p\right)_s. \tag{10}$$

Here, $u_D^{(p)}$ and $v_D^{(p)}$ denote the Darcy (superficial) velocity components in the porous region. Under the LTE assumptions, the fluid and solid phases share a common temperature, while the effects of porosity on the thermal transport are represented through the volume-averaged effective properties k_{eff} and $\left(\rho C_p\right)_{eff}$. Since the present analysis is steady, no transient thermal storage term appears in the energy equation.

Since the porous baffles are fully saturated with the electrically conducting THNF, the fluid moving through the interconnected pore space is also subjected to the externally imposed magnetic field. Therefore, the momentum equations in the porous region include the Lorentz force contribution in addition to the Darcy and Forchheimer resistance terms. The Darcy and Forchheimer terms represent the hydrodynamic resistance imposed by the porous matrix, whereas the Lorentz force term represents magnetic damping of the electrically conducting fluid occupying the pore space.

2.2.3. Nondimensional governing equations

The system of Eqs (1)–(8) above is rendered dimensionless using the following scaling variables:

$$X = \frac{x}{L}, Y = \frac{y}{L}, U = \frac{u}{u_0}, V = \frac{v}{u_0}, P = \frac{p}{\rho_{thnf} u_0^2}, \theta = \frac{T - T_c}{T_h - T_c}. \tag{11}$$

The dimensionless quantities are introduced as follows:

Reynolds number $\left(Re = {(u_0 L)}/{\upsilon_{thnf}}\right)$, Prandtl number $\left(Pr = {\upsilon_{thnf}}/{\alpha_{thnf}}\right)$, Peclet number $\left(Pe = RePr = {u_0 L}/{\alpha_{thnf}}\right)$, $Ha = B_0 L\sqrt{\frac{\sigma_{thnf}}{\mu_{thnf}}}$, $R_c = \frac{k_{eff}}{k_{thnf}}$ and Darcy number $\left(Da = {K}/{L^2}\right)$.

In the present study, changing the Da means changing only the porous fins' permeability K. Although all selected Das are smaller than unity, this does not mean that the flow is treated as a pure Darcy flow. A small Da indicates low permeability and strong porous resistance. In the present work, the Darcy–Brinkman–Forchheimer model is used instead of the pure Darcy model because viscous diffusion near the porous fins' boundaries and inertial resistance inside the porous fins are considered.

2.2.4. Dimensionless equations in the clear fluid region

$$\frac{\partial U^{(f)}}{\partial X} + \frac{\partial V^{(f)}}{\partial Y} = 0. \tag{12}$$

$$U^{(f)} \frac{\partial U^{(f)}}{\partial X} + V^{(f)} \frac{\partial U^{(f)}}{\partial Y} = -\frac{\partial P^{(f)}}{\partial X} + \frac{1}{Re}\left(\frac{\partial^2 U^{(f)}}{\partial X^2} + \frac{\partial^2 U^{(f)}}{\partial Y^2}\right) - \frac{Ha^2}{Re} U^{(f)}. \tag{13}$$

$$U^{(f)} \frac{\partial V_f}{\partial X} + V^{(f)} \frac{\partial V^{(f)}}{\partial Y} = -\frac{\partial P^{(f)}}{\partial Y} + \frac{1}{Re}\left(\frac{\partial^2 V^{(f)}}{\partial X^2} + \frac{\partial^2 V^{(f)}}{\partial Y^2}\right). \tag{14}$$

$$U^{(f)} \frac{\partial \theta^{(f)}}{\partial X} + V^{(f)} \frac{\partial \theta^{(f)}}{\partial Y} = \frac{1}{Re\, Pr}\left(\frac{\partial^2 \theta^{(f)}}{\partial X^2} + \frac{\partial^2 \theta^{(f)}}{\partial Y^2}\right). \tag{15}$$

2.2.5. Dimensionless equations in the porous fin region

$$\frac{\partial U^{(p)}}{\partial X} + \frac{\partial V^{(p)}}{\partial Y} = 0. \tag{16}$$

$$\begin{aligned} \frac{1}{\varepsilon^2}\left(U^{(p)} \frac{\partial U^{(p)}}{\partial X} + V^{(p)} \frac{\partial U^{(p)}}{\partial Y}\right) = -\frac{\partial P^{(p)}}{\partial X} + \frac{1}{\varepsilon Re}\left(\frac{\partial^2 U^{(p)}}{\partial X^2} + \frac{\partial^2 U^{(p)}}{\partial Y^2}\right) - \frac{1}{ReDa} U^{(p)} - \\ \frac{C_F}{\sqrt{Da}}\left(\sqrt{U^{(p)^2} + V^{(p)^2}}\right) U^{(p)} - \frac{Ha^2}{Re} U^{(p)}. \end{aligned} \tag{17}$$

$$\begin{aligned} \frac{1}{\varepsilon^2}\left(U^{(p)} \frac{\partial V^{(p)}}{\partial X} + V^{(p)} \frac{\partial V^{(p)}}{\partial Y}\right) = -\frac{\partial P^{(p)}}{\partial Y} + \frac{1}{\varepsilon Re}\left(\frac{\partial^2 V^{(p)}}{\partial X^2} + \frac{\partial^2 V^{(p)}}{\partial Y^2}\right) - \frac{1}{ReDa} V^{(p)} - \\ \frac{C_F}{\sqrt{Da}}\left(\sqrt{U^{(p)^2} + V^{(p)^2}}\right) V^{(p)}. \end{aligned} \tag{18}$$

$$U^{(p)}\frac{\partial\theta^{(p)}}{\partial X}+V^{(p)}\frac{\partial\theta^{(p)}}{\partial Y}=\frac{R_c}{Pe}\left(\frac{\partial^2\theta^{(p)}}{\partial X^2}+\frac{\partial^2\theta^{(p)}}{\partial Y^2}\right). \tag{19}$$

2.2.6. Boundary conditions

The associated boundary conditions for the present physical domain, illustrated in Figure 1, are specified as follows.

At the inlet: $X=0,-1\le Y\le 1$

$$U=1,\ V=0,\ \theta=0. \tag{20}$$

At the outlet: $X=23,-1\le Y\le 1$

$$P=0,\ \frac{\partial U}{\partial X}=0,\ \frac{\partial V}{\partial X}=0,\ \frac{\partial\theta}{\partial X}=0. \tag{21}$$

At the heated wavy walls: $3\le X\le 18$

$$U=0,\ V=0,\ \theta=1. \tag{22}$$

At the straight adiabatic walls: $0\le X<3$ and $18<X\le 23$

$$U=0,\ V=0,\ \frac{\partial\theta}{\partial N}=0. \tag{23}$$

At the clear fluid–porous baffle interfaces

The continuity of velocity, pressure, temperature, and heat flux is set as follows:

$$U^{(f)}=U^{(p)},\ V^{(f)}=V^{(p)},\ P^{(f)}=P^{(p)},\ \theta^{(f)}=\theta^{(p)}. \tag{24}$$

At the interfaces separating the clear fluid region from the porous fins, the continuity of velocity, shear stress, temperature, and heat flux is inherently satisfied through the Darcy–Brinkman formulation and apparent thermal conductivity model used in the energy equation.

2.2.7. Hydrothermal characteristics

The local and average Nusselt number, pressure drop, and hydraulic performance index are used to quantify the hydrothermal behavior of the system.

The local Nusselt number is defined using the thermal conductivity of the base fluid, k_f, as the reference conductivity. From Fourier's law $q''=k_{thnf}\,\partial T/\partial n$ and the definition $Nu_{local}=q''L/\left[k_f(T_h-T_c)\right]$, the dimensionless local Nusselt number is obtained as follows:

$$Nu_{local}=-\frac{k_{thnf}}{k_f}\frac{\partial\theta}{\partial n}\Big|_{wavy\ wall}. \tag{25}$$

Therefore, the factor $\frac{k_{thnf}}{k_f}$ accounts for the modification of thermal conductivity caused by the suspended nanoparticles and is not included in the definition of the dimensionless temperature θ.

The average Nusselt number over the upper and lower wavy wall can be evaluated by the integration of Nu_{local}.

$$Nu_{avg} = \frac{1}{S_h}\int_{T_h} Nu_{local}\, dS. \tag{26}$$

Here, $S_h = \int_{T_h} dS$ is the total dimensionless arc length of the heated wavy walls.

The dimensionless drop in static pressure (ΔP) across the channel is defined as the difference between the area-averaged static pressure at the inlet and outlet of the channel

$$\Delta \mathrm{P} = P_{in} - P_{out}, \tag{27}$$

where $P_{in} = \frac{1}{A_{in}}\int_{A_{in}} P\, dA$ and $P_{out} = \frac{1}{A_{out}}\int_{A_{out}} P\, dA$.

Here, P denotes the dimensionless static pressure.

To assess the overall interaction between thermal enhancement and hydraulic loss, a thermo-hydraulic performance index (PI) is introduced. This index compares the increase in Nu_{avg} with the corresponding variation in Δp relative to a reference configuration. A value of $PI > 1$ indicates that the tested configuration provides better overall thermo-hydraulic performance than the reference case.

$$PI = \frac{{}^{Nu_{avg}}/_{Nu_{avg,ref}}}{\left({}^{\Delta \mathrm{P}}/_{\Delta \mathrm{P}_{ref}}\right)^{1/3}}. \tag{28}$$

2.2.8. Thermophysical properties of the THNF

Cu, CuO, and Al_2O_3 nanoparticles are considered because their different thermophysical properties provide a representative ternary hybrid combination for enhancing thermal transport. In particular, the high thermal conductivity of Cu is combined with the thermal characteristics of the metal oxide nanoparticles CuO and Al_2O_3. Their individual contributions are incorporated through the adopted ternary mixture's property relations. The thermophysical properties of the Cu–CuO–Al_2O_3/water THNF are evaluated using standard mixture correlations [38]. The density and heat capacity are given as follows:

$$\rho_{thnf} = (1-\phi)\rho_{bf} + \phi_1\rho_{s1} + \phi_2\rho_{s2} + \phi_3\rho_{s3}. \tag{29}$$

$$\left(\rho C_p\right)_{thnf} = (1-\phi)\left(\rho C_p\right)_{bf} + \phi_1\rho\left(\rho C_p\right)_{s1} + \phi_2\left(\rho C_p\right)_{s2} + \phi_3\rho\left(\rho C_p\right)_{s3}. \tag{30}$$

The dynamic viscosity is calculated using the Brinkman correlation

$$\mu_{thnf} = \frac{\mu_{bf}}{(1-\phi)^{2.5}} \tag{31}$$

In the Brinkman formulation, the viscosity enhancement depends on the total solid volume fraction rather than the chemical identity of each particle constituent. Accordingly, Cu, CuO, and Al_2O_3 are treated collectively in the viscosity relation through $\phi = \phi_1 + \phi_2 + \phi_3$. This

approximation assumes a homogenous and well-dispersed dilute suspension and neglects species-specific particle size, morphology, aggregation, and particle–particle interaction effects. Similar extensions based on the total nanoparticle loading have been used for HNFs in previous studies [39].

The equivalent thermal conductivity of three nanoparticles constituents is evaluated using a volume-fraction-weighted harmonic mixing rule, which represents a series-type effective medium approximation. Harmonic averaging provides a conservation estimate of the effective conductivity of heterogenous constituents and has been used in the effective thermal conductivity formulation for multiphase media [40]. The resulting equivalent nanoparticle conductivity is subsequently incorporated into the Maxwell relation to evaluate the thermal conductivity of the THNF.

$$k_{p,eff} = \frac{\phi}{\frac{\phi}{k_{s1}}+\frac{\phi}{k_{s2}}+\frac{\phi}{k_{s3}}}. \tag{32}$$

$$\frac{k_{thnf}}{k_{bf}} = \frac{k_{p,eff}+2k_{bf}-2\phi(k_{bf}-k_{p,eff})}{k_{p,eff}+2k_{bf}+\phi(k_{bf}-k_{p,eff})}. \tag{33}$$

This mixing rule does not explicitly account for synergistic, aggregation, differences in particle size, or interfacial thermal resistance among the three nanoparticle species. It is therefore adopted as an effective continuum approximation for the dilute and uniformly dispersed ternary suspension considered here.

The electrical conductivity of the THNF is subsequently obtained from

$$\frac{\sigma_{thnf}}{\sigma_{bf}} = \frac{\sigma_{p,eff}+2\sigma_{bf}-2\phi(\sigma_{bf}-\sigma_{p,eff})}{\sigma_{p,eff}+2\sigma_{bf}+\phi(\sigma_{bf}-\sigma_{p,eff})}. \tag{34}$$

Here, $\phi = \phi_1 + \phi_2 + \phi_3$ is the total volume fraction, where ϕ_1, ϕ_2, ϕ_3 correspond to the individual volume fraction of Cu, CuO, and Al_2O_3 nanoparticles, respectively. An equal volume distribution is considered for the three nanoparticle species. The subscripts bf and s_i represent the base fluid and the individual nanoparticle types. Table 1 summarizes the key thermophysical characteristics of the host liquid (water) and the constituent nanoparticles, including Cu, CuO, and Al_2O_3, which are used in the present THNF formulation.

Table 1. Thermo-physical properties of the THNF [41].

Physical properties	Water (bf)	Cu (s1)	CuO (s2)	Al_2O_3 ($s3$)
Density, ρ (kg m^{-3})	997.1	8933	6320	3970
Specific heat, C_p (J kg^{-1}k^{-1})	4179	385	531.8	765
Thermal conductivity, k (W m^{-1} K^{-1})	0.613	401	76.5	40
Electrical conductivity σ (S m^{-1})	5.5×10^{-6}	5.8×10^{7}	1.6×10^{-1}	6.78×10^{-10}

3. Numerical methodology and code procedures

3.1. Numerical procedure

The mathematical model comprising Eqs (12)–(19), together with the boundary conditions

specified in Eqs (20)–(24), is solved numerically using the FEM. The FEM was selected because of its flexibility in handling complex corrugated geometries, porous regions, and coupled multiphysics equations. Compared with conventional structured grid approaches, FEM enables accurate discretization of the corrugated walls and porous baffle boundaries. All computations are carried out in COMSOL Multiphysics 6.3, a commercial finite element platform. The computational domain is divided into unstructured triangular elements because they can accurately conform to the corrugated boundaries and porous baffle geometry while allowing localized mesh refinement in regions with large velocity and temperature gradients.

The FEM provides a piecewise approximation of the solution field using triangular finite elements with three nodes per element. The computational mesh is based on this structure. Applying the method of weighted residuals to the equations yields a weak form of the equations. The weak form of the equations is written as a variational problem by defining an appropriate set of trial functions. The dependent field variables, like temperature θ, pressure P, and the velocity components U and V are approximated as linear combinations of the shape functions within each finite element, and these are substituted into the variational form of the equations to form equations for each element.

From this, local element matrices are formed via numerical integration and assembled to form a global system matrix for the domain. A fully coupled damped Newton solver based on a direct linear solver (PARDISO) for robustness to convergence is utilized iteratively to solve the nonlinear system of algebraic equations resulting from the simulation. The coupled solver is used to solve the flow–temperature field interaction and capture the thermo-fluidic behavior accurately when porous fins are used. The convergence tolerance for all the dependent variables (temperature, pressure, and velocity) is chosen as a relative tolerance of 10^{-6}.

The porous fins are simulated using the Darcy–Brinkman–Forchheimer formulation, which accounts for shear stresses due to viscous shear (Brinkman term) and the bulk flow indicator (Darcy term). Continuity of velocity, tangential stress, temperature, and conductive heat flux is automatically satisfied at the clear fluid–porous interfaces by the weak formulation. The porous fins have LTE.

3.2. Mesh generation and grid independence

An unstructured triangular finite element mesh was used to discretize the computational domain, as shown in Figure 2. To adequately capture the steep velocity and temperature gradients, local mesh refinement was applied near the heated corrugated walls, porous baffles and fluid–porous interface, while a relatively coarser mesh was used in the remaining regions to reduce the computational cost. The mesh selected for the present simulations consists of 98,272 triangular elements.

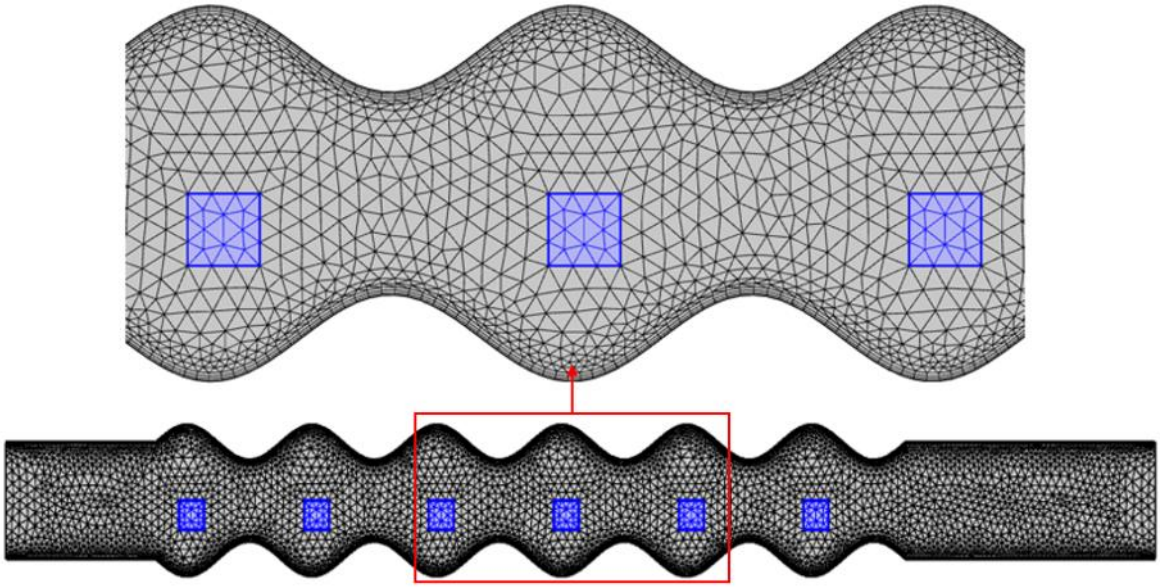


Figure 2. Finite element mesh with 98,272 elements.

A grid independence test was carried out for the reference case of $Da = 10^{-3}, Re = 100, \phi = 0.03,$ and $\epsilon = 0.6$. Four progressively refined triangular meshes were examined and Nu_{avg} was selected as the convergence indicators. The successive relative difference was calculated as $E_i = |Nu_i - Nu_{i-1}| / |Nu_{i-1}| \times 100$. As presented in Table 2, Nu_{avg} approaches a stable value as the mesh is refined. Although the relative differences between the coarser mesh levels are nonmonotonic, the difference between the two finest meshes, M3 and M4, decreases to approximately 0.52%. This indicates that further refinement from 98,272 to 165,562 elements produces only a minor change in Nu_{avg}. Therefore, M3 containing 98,272 triangular elements, was adopted for the subsequent simulations as a compromise between numerical accuracy and computational cost.

Table 2. Grid independence test for $Da = 10^{-3}, Re = 100, \phi = 0.03,$ and $\epsilon = 0.6$.

Mesh	No. of elements	Nu_{avg}	Successive relative difference (%)
M1	15,550	3.6087	–
M2	39,358	3.5494	1.64%
M3	98,272	3.4207	3.63%
M4	165,562	3.4029	0.52%

3.3. Solver convergence

Figure 3 presents the convergence history of the fully coupled nonlinear solver for a representative computational case. The solver error decreases continuously by several orders of magnitude, from above 10^1 at the initial iteration to approximately 10^{-8} after 10 iterations. The smooth and rapid reduction in the error without noticeable oscillations demonstrates the stable convergence of the coupled numerical solution. Together with the grid's independence and the model validation results, this convergence behavior supports the numerical reliability of the present FEM computations.

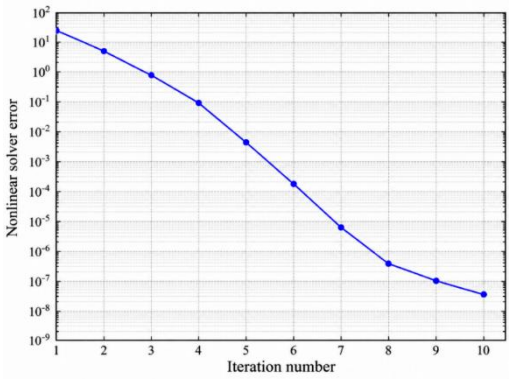


Figure 3. Convergence history of the fully coupled nonlinear FEM solver.

3.4. Model validation

The accuracy of the present numerical procedure was assessed through both qualitative and quantitative comparisons with the published results of Hamza et al. [36]. First, the streamlines patterns for the mid-center line (MCL) configuration at $Re = 25$ and $Re = 250$ were reproduced, showing close agreement in the principal flow structures and recirculation regions (Figure 4(a)). In addition, a quantitative comparison of Nu_{avg} was performed over the considered Re range under the corresponding reference conditions. As shown in Figure 4(b), the present FEM predictions closely follow the results reported by Hamza et al., providing further evidence of the accuracy and reliability of the numerical model. This validated solver is subsequently extended to investigate the thermo-hydraulic performance of the corrugated channel equipped with porous baffles.

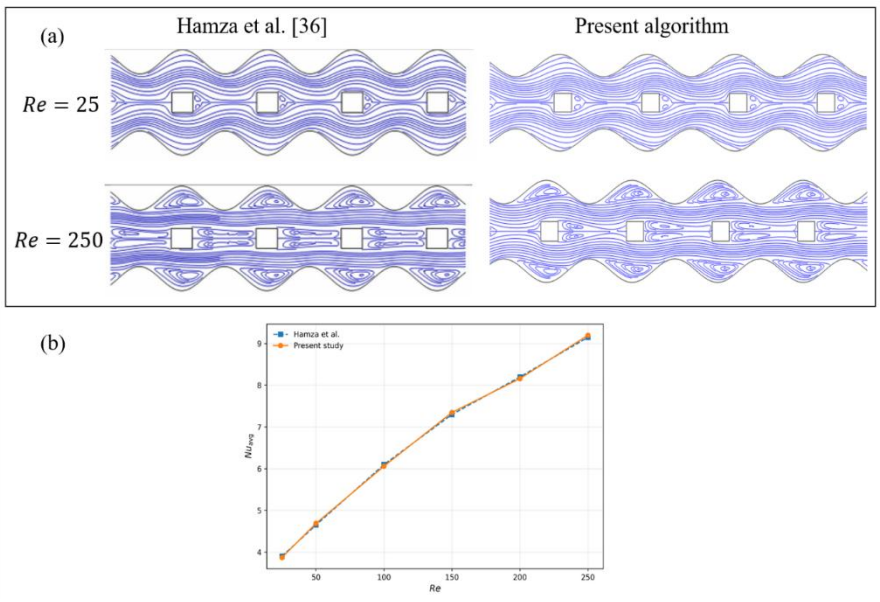


Figure 4. (a) Comparison of the streamlines' contours predicted by the present numerical model with the refernce results of Hamza et al. [36] for a corrugated channel with solid obstacles at $Ha = 0$ and $\phi = 0.03$. **(b)** Comparison of the average Nusselt number obtained from the present FEM model with the numerical results of Hamza et al. [36] for the MCL configuration at $Ha = 0$ and $\phi = 0$.

4. Numerical analysis and discussion

This section discusses the numerical outcomes for laminar MHD forced convection of a Cu–CuO–Al_2O_3/water THNF flowing through a corrugated channel equipped with porous baffles. The effects of Da, Re, the volume fraction of nanoparticles (ϕ), and the Ha are analyzed in terms of the flow structure, temperature distribution, average Nusselt number (Nu_{avg}), pressure drop (ΔP), and thermo-hydraulic performance index (PI). Initially, the thermal and hydraulic performances of the solid baffle channel and the porous baffle channel are compared to evaluate the influence of baffle permeability on heat transfer enhancement and pressure-drop reduction. Subsequently, the effects of the governing dimensionless parameters are analyzed for the selected porous baffle configuration to identify the conditions that provide the best overall thermo-hydraulic performance.

Figure 5 compares the streamline distributions for the solid baffle and porous baffle channels at $(Re = 100)$ and $(Re = 200)$ with $(Ha = 0)$ and $(\phi = 0.03)$. In the case of porous baffles, the Da and porosity are fixed at $Da = 10^{-3}$, and $\epsilon = 0.6$ respectively. For the solid baffle channel, the fluid is completely blocked by the impermeable baffles, resulting in large recirculation zones downstream of each baffle. As the Re increases from 100 to 200, the wake regions become longer and the vortices intensify due to the stronger inertial effects. Conversely, the presence of porous baffles enables partial fluid penetration into the porous matrix, thereby weakening the flow's separation and significantly reducing the size of the downstream recirculation zones. Consequently, the streamlines become smoother and more uniformly distributed throughout the channel. The reduced wake formation in the porous baffle channel indicates a lower flow resistance than that of the solid baffle channel, leading to a smaller pressure drop while maintaining effective flow disturbance. These observations demonstrate that replacing solid baffles with porous baffles provides a better balance between heat transfer enhancement and hydraulic performance.

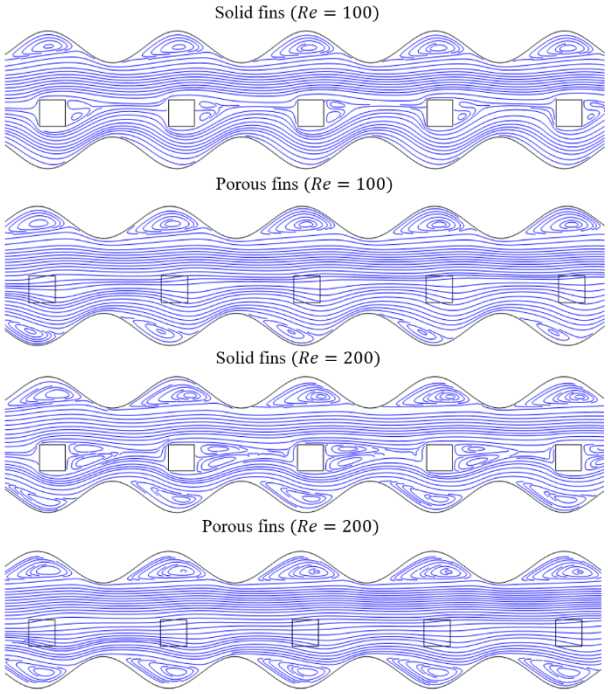


Figure 5. Streamlines for the solid baffle channel (top row) and the porous baffle channel (bottom row) for Re at , $\phi = 0.03$ and $Ha = 0.0$. For the porous fin case, $Da = 10^{-3}$ and $\epsilon = 0.6$.

Figure 6 presents the isotherm lines for the solid baffle and porous baffle channels at Re = 100 and Re = 200. For both Re, the solid baffles interrupt the flow and create relatively thicker thermal boundary layers downstream of the baffles. In contrast, the porous baffles allow partial fluid penetration through the porous medium, resulting in stronger fluid mixing and a better-distributed temperature field within the channel. Consequently, the temperature gradient layer becomes thinner around the porous baffles, revealing intensified convective transport. Increasing the Re from 100 to 200 further intensifies the convective transport, leading to a tighter concentration of isotherms near the heated corrugated surfaces and more uniformly distributed throughout the flow field. Compared with the solid baffle channel, the porous baffle channel exhibits more effective thermal mixing and a thinner temperature gradient layer, leading to an improvement in the overall thermal transport performance.

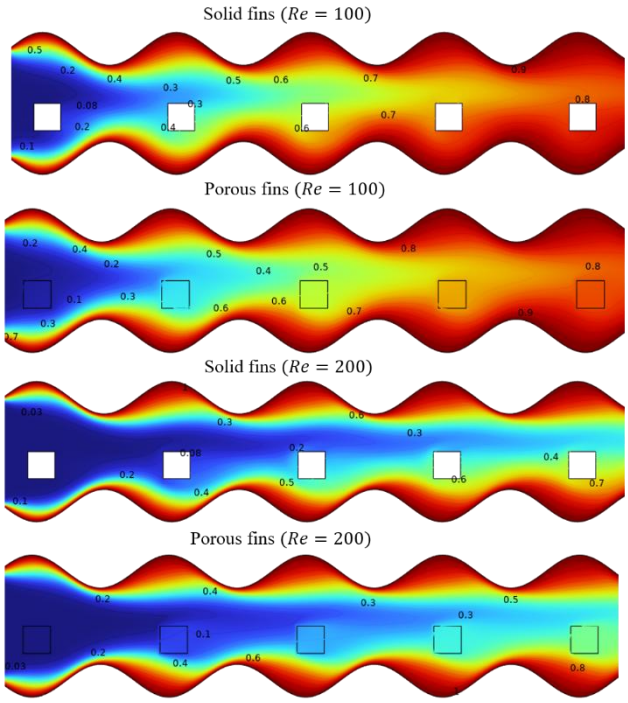


Figure 6. Isotherms contours for the solid baffle channel (top row) and the porous baffle channel (bottom row) for Re at , $\phi = 0.03$ and $Ha = 0.0$. For the porous fin case, $Da = 10^{-3}$ and $\epsilon = 0.6$.

Figure 7 illustrates the variations in Nu_{avg} and ΔP with Re for the solid baffle and porous baffle channels. As evident from Figure 7(a), the Nu_{avg} increases continuously with Re for both configurations due to the enhanced thermal energy transport. However, the porous baffle channel consistently yields a higher Nu_{avg} than the solid baffle channel over the entire Re range. At Re = 250, the porous baffles increase the Nu_{avg} from 10.849 to 11.332, corresponding to an enhancement of approximately 4.45%. This improvement is attributed to the penetration of the fluid through the porous baffles, thereby promoting stronger fluid circulation and reducing the thickness of the near-wall thermal layer.

Figure 7(b) shows that ΔP decreases with rising Re for both channels. Furthermore, the porous baffle channel consistently exhibits a lower pressure drop than the solid baffle channel because the

fluid partly passes through the porous medium instead of completely bypassing the impermeable baffles. At Re = 250, the pressure drop decreases from 8.1812 for the solid baffle channel to 7.0996 for the porous baffle channel, representing a reduction of approximately 13.22%. These results demonstrate that porous baffles simultaneously enhance heat transfer and reduce flow resistance, thereby providing superior thermo-hydraulic performance compared with conventional solid baffles.

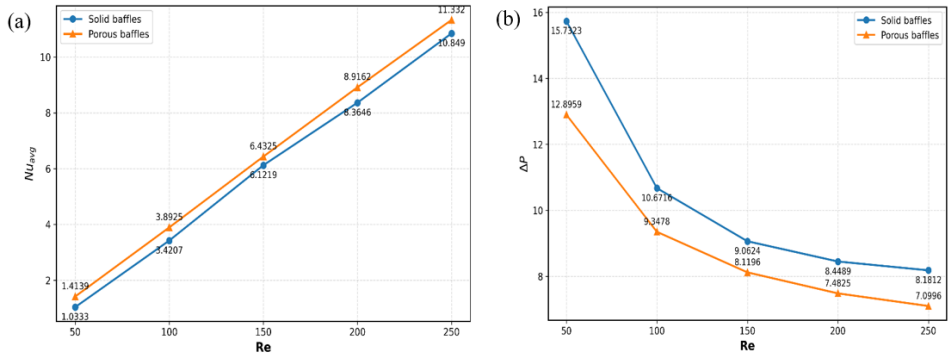


Figure 7. Variation of (a) Nu_{avg} and (b) ΔP with Re for the solid baffle channel and the porous baffle channel.

Figure 8 presents the streamline and isotherm contours for the porous baffle channel at $Da = 10^{-6}$ and $Da = 10^{-3}$. The Da serves as a measure of the permeability of the porous baffle matrix; therefore, increasing Da reduces the flow resistance inside the porous structure. As shown in the streamline contours, increasing the Da from 10^{-6} to 10^{-3} allows more fluid to penetrate through the porous baffles, resulting in smoother streamlines and weaker recirculation regions downstream of the baffles. The reduced flow obstruction improves the overall flow uniformity and decreases the hydraulic resistance of the channel. The strong dependence of the thermo-hydraulic response on Da is consistent with previous porous medium studies demonstrating that permeability substantially alters fluid transport and the associated heat transfer characteristics [35]. The corresponding isotherm contours indicate that a higher Da enhances fluid mixing around the porous baffles, hereby reducing the thickness of the near-wall thermal layer. and a more uniform temperature distribution. Consequently, heat is transported more effectively from the heated corrugated walls to the core flow. These observations demonstrate that increasing the permeability of the porous baffles improves both the hydrodynamic behavior and the convective heat transfer performance while reducing the pressure drop penalty.

Figure 9 illustrates the variations in Nu_{avg} and ΔP with Da for the porous baffle channel at $Re = 100, \phi = 0.03, Ha = 10,$ and $\epsilon = 0.6$. As shown in Figure 9(a), the Nu_{avg} increases with increasing Da. At low permeability (10^{-6} and 10^{-5}), the porous baffles behave similarly to impermeable obstacles, resulting in only a slight improvement in heat transfer. As the Da rises to $10^{-3}$and 10^{-2}, the elevated permeability of the porous baffles permits increased fluid permeation through the porous matrix, fostering stronger fluid mixing and diminishing the thermal boundary layer's thickness. Consequently, the convective thermal transport is intensified, resulting in a pronounced increase in Nu_{avg}. The maximum Nu_{avg} of 2.7172 is obtained at 10^{-2}. Figure 9(b) shows that the pressure drop decreases continuously with a rising Da due to the reduction in flow resistance within the porous baffles. Increasing the Da from 10^{-6} to 10^{-2} reduces the pressure

drop from 24.6520 to 22.3450, corresponding to a reduction of approximately 9.36%. Therefore, raising the permeability of the porous baffles simultaneously enhances heat transport and lowers the hydraulic resistance, resulting in improved thermo-hydraulic performance.

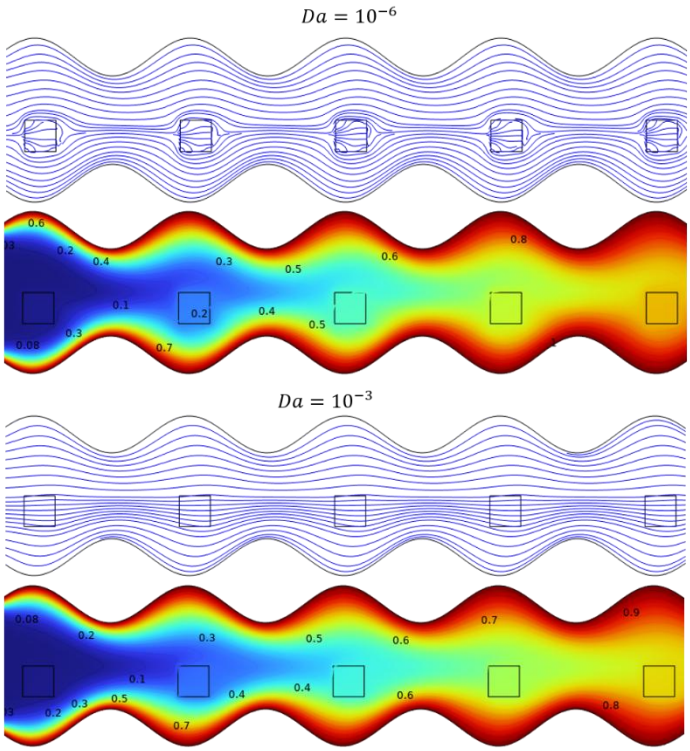


Figure 8. Streamlines (top row) and isotherm contours (bottom row) for selected Da values in the porous baffle channel at $Re = 100,\ \phi = 0.03,\ Ha = 10,$ and $\epsilon = 0.6$.

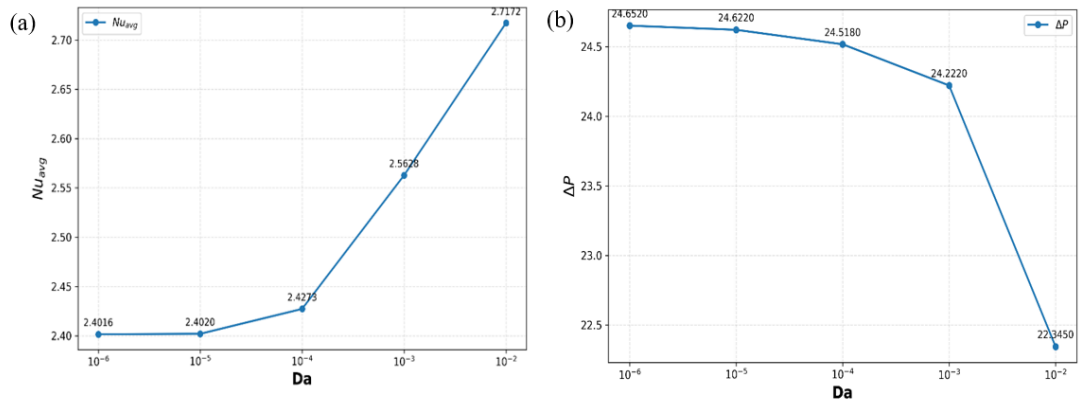


Figure 9. Variation in (a) Nu_{avg} and (b) ΔP with Da for the porous baffled channel.

Figure 10 presents the streamline and isotherm contours for the porous baffle channel at Ha = 0 and Ha = 40. The Ha represents the strength of the applied magnetic field and its influence on the electrically conducting THNF. As shown in the streamline contours, increasing the Ha from 0 to 40 suppresses the fluid's motion due to the Lorentz force acting opposite to the flow direction. Consequently, the streamline's density decreases around the porous baffles, and the recirculation

regions become weaker, indicating a more stabilized flow field. Similar magnetic suppression of fluid motion has been reported for MHD THNFs in porous configurations [33]. The corresponding isotherm contours reveal that the stronger magnetic field reduces fluid mixing and weakens convective cooling performance, resulting in a thicker thermal layer and a more gradual temperature distribution along the channel. As a result, the transport of heat from the heated corrugated walls to the core flow is reduced. These observations indicate that increasing the Ha suppresses convection and consequently deteriorates the overall thermal enhamcment of the porous baffle channel.

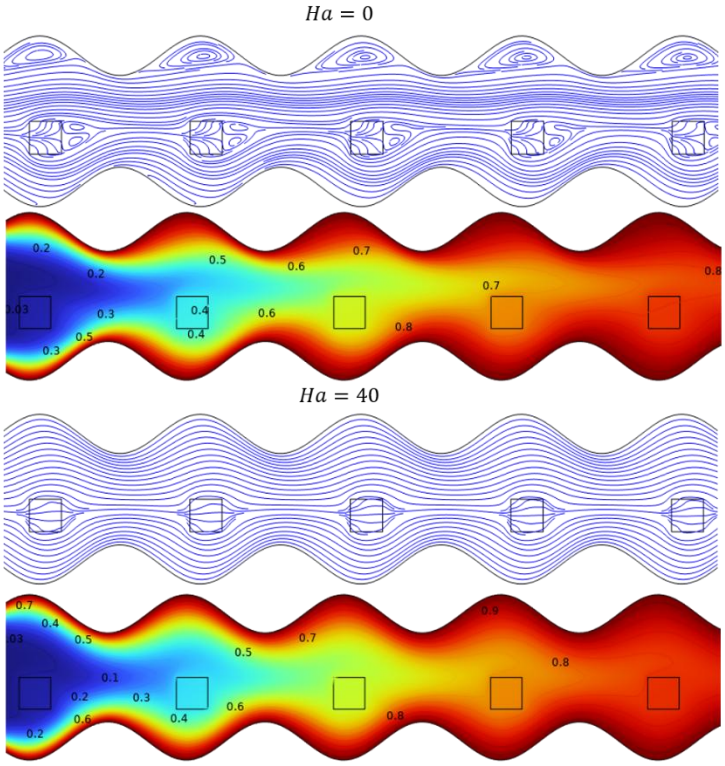


Figure 10. Streamlines (top row) and isotherms contours (bottom row) for selected Ha values in the porous baffle channel at $Re = 100, \phi = 0.03,\ Da = 10^{-3}$, and $\epsilon = 0.6$.

Figure 11 illustrates the evolution of Nu_{avg} and ΔP with Ha and the nanoparticle volume fraction for the porous baffle channel. As shown in Figure 11(a,b), increasing the Ha significantly decreases the Nu_{avg} while increasing the pressure drop. The electromagnetic force generated by the applied magnetic field restricts the fluid's movement, weakens convective mixing, and broadens the thermal diffusion layer, resulting in lower heat transfer rates. Consequently, Nu_{avg} decreases from 3.8925 at Ha = 0 to 0.5992 at Ha = 40, whereas the pressure drop increases markedly from 11.0504 to 216.3916. Figure 11(c, d) presents the influence of ϕ. Increasing ϕ enhances the effective heat conduction capability of the THNF, leading to a continuous increase in Nu_{avg}. At the same time, an increase in the nanoparticle concentration raises the effective viscosity of the working fluid, resulting in a higher pressure drop. As ϕ rises from 0.00 to 0.03, Nu_{avg} increases from 0.3429 to 2.4272, while the pressure drop rises from 9.9860 to 21.9621. These results indicate that raising ϕ improves the heat transfer performance at the expense of additional hydraulic resistance.

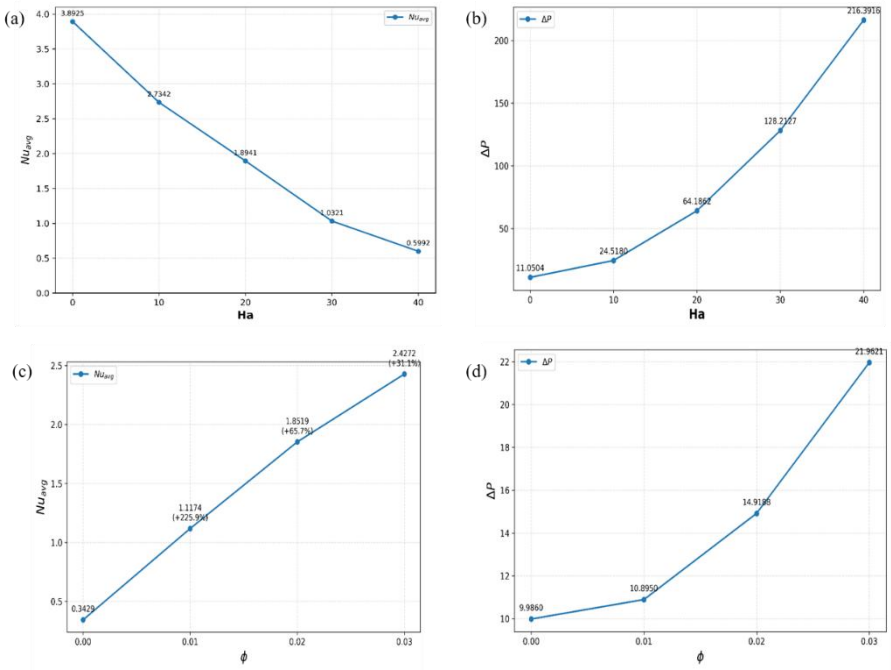


Figure 11. Variation in (a) Nu_{avg} and (b) ΔP with Ha and ϕ for the porous baffle channel.

Figure 12 presents the vertical cutline profiles of the dimensionless velocity components U and V, temperature (θ), and the Nusselt number for different values of Da. Figure 12(a,b) shows that increasing the Da slightly modifies the velocity profiles due to the higher permeability of the porous baffles. At $Da = 10^{-2}$, the fluid penetrates more easily through the porous medium, resulting in smoother U- and V-velocity distributions and weaker flow disturbance compared with a lower Da. Figure 12(c) illustrates the dimensionless temperature profiles along the vertical cutline. Increasing the Da reduces the fluid temperature throughout most of the channel because the enhanced permeability promotes stronger fluid mixing and convective heat transport. The corresponding Nusselt number distributions are shown in Figure 12(d). Distinct peaks are observed near the heated corrugated wall, where the local temperature gradients are highest. As the Da increases, the Nusselt number increases over most of the heated wall, with the highest values obtained at $Da = 10^{-2}$. This behavior confirms that increasing the permeability of the porous baffles enhances the local heat transfer rate by strengthening fluid penetration and reducing the thermal boundary layer's thickness.

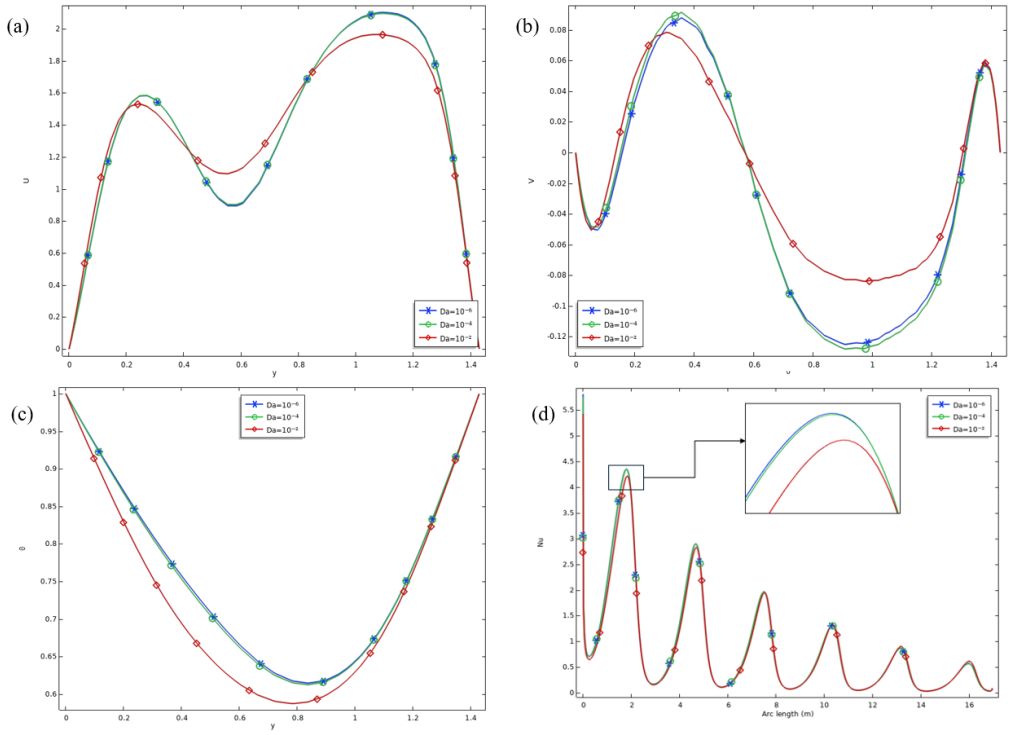


Figure 12. Vertical cutline profiles of (a) U-velocity, (b) V-velocity, (c) temperature (θ), and (d) variation in the local Nusselt number (Nu) along the upper wavy heated wall for different values of Da at $Re = 100, \epsilon = 0.6,$ and $\phi = 0.03$.

Figure 13 presents the thermo-hydraulic performance index for the porous baffle channel. In Figure 13(a), the solid baffle channel is selected as the reference case, whereas in Figure 13(b), the porous baffle case at $Da = 10^{-6}$ is taken as the reference. As shown in Figure 13(a), the porous baffle channel yields PI > 1 over the entire Re range, indicating superior overall thermo-hydraulic performance compared with the solid baffle channel. The highest performance index of 1.462 is obtained at Re = 50, corresponding to a 46.2% improvement over the solid baffle configuration. Although the performance index decreases slightly with an increasing Re, it consistently exceeds unity under all investigated conditions, confirming that the porous baffles simultaneously improve heat removal capabilty while reducing the pressure drop penalty. Figure 13(b) illustrates the effects of the Da on the thermo-hydraulic performance of the porous baffle channel. The performance index increases monotonically from 1.000 at $Da = 10^{-6}$ to 1.169 at $Da = 10^{-2}$. This trend suggests that increasing the permeability of the porous baffles facilitates greater fluid permeation through the porous matrix, thereby promoting convective thermal transport while reducing hydraulic resistance. Consequently, the porous baffle channel achieves its best overall thermo-hydraulic performance at the highest Da considered, i.e., $Da = 10^{-2}$.

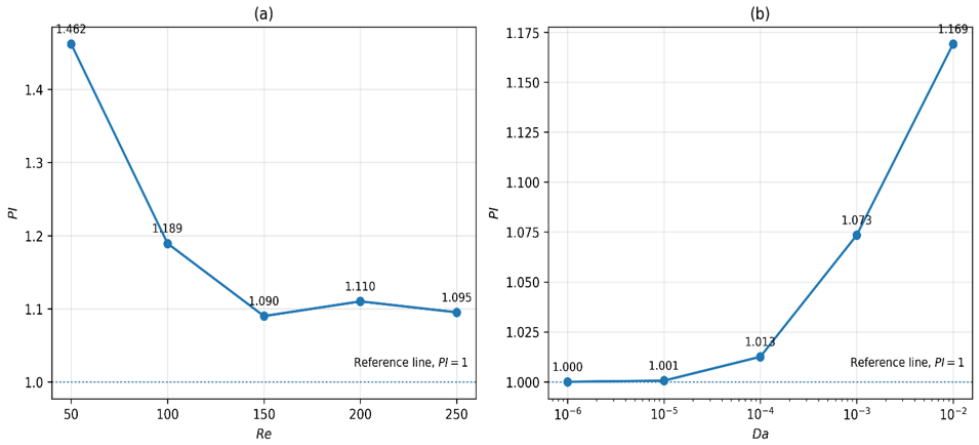


Figure 13. Thermo-hydraulic performance index (PI) for (a) porous fins relative to solid fins at different values of Re, and (b) the porous baffle Da using $Da = 10^{-6}$ as the reference case.

5. ANN analysis

To complement the numerical simulations, an ANN was developed as a data-driven surrogate for reproducing the FEM-computed thermo-hydrodynamic responses. The input vector consists of the spatial coordinates together with the governing parameters, namely x or (s), $Re, Ha, Da, \epsilon,$ and ϕ. Separate feedforward neural networks were trained to estimate the U-velocity, V-velocity, dimensionless temperature (θ), and local Nusselt number. As demonstrated in Figure 14, each network consists of two fully connected hidden layers with 10 neurons per layer. The hyperbolic tangent sigmoid activation function was used in both hidden layers, while a linear purelin function was used at the output layer. The networks were trained using the Levenberg–Marquart algorithm, with the available data divided into 70% for training, 15% for validation, and 15% for testing. Model performance is evaluated using mean square error (MSE) learning curves, regression analysis, prediction error distribution, residual analysis, and direct comparisons between FEM and ANN estimates. The inclusion of the governing parameters as ANN inputs enables the surrogate to account for both spatial and parametric variations within the investigated FEM database.

Figure 15 presents the evolution of the training and validation MSE for U, V, θ, and Nusselt number. For all predicted quantities, the MSE decreases rapidly during the initial epochs and subsequently approaches a low, nearly stable level. More importantly, the training and validation curves remain closely aligned without substantial divergence, indicating stable convergence and no evident deterioration in the validation performance. The rapid convergence observed for temperature together with the consistently low final errors for all outputs, demonstrates effective learning of the numerical relationships by the ANN.

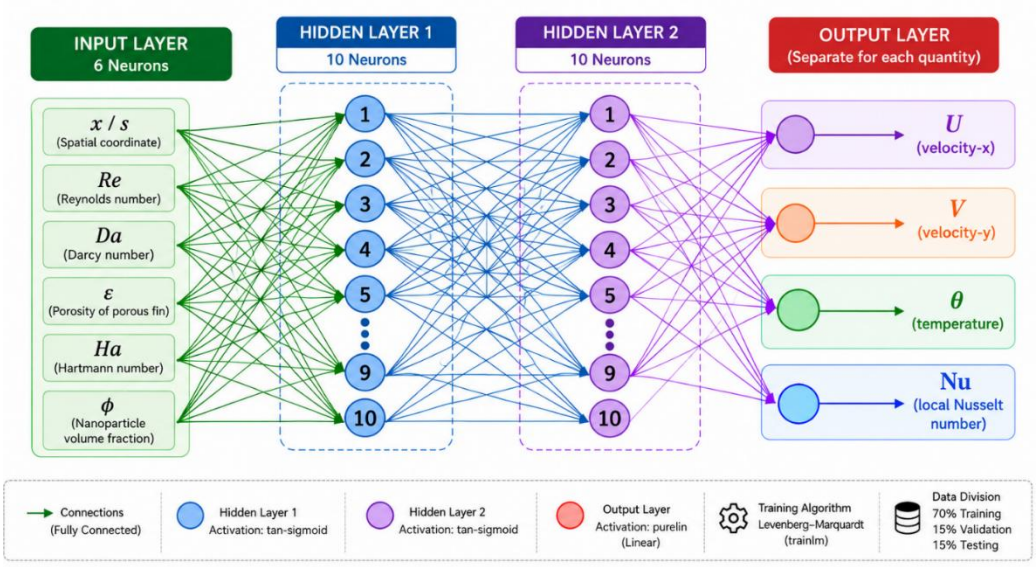


Figure 14. Architecture of the feedforward ANN used separately used for predicting the U-velocity, V-velocity, temperature, and local Nusselt number.

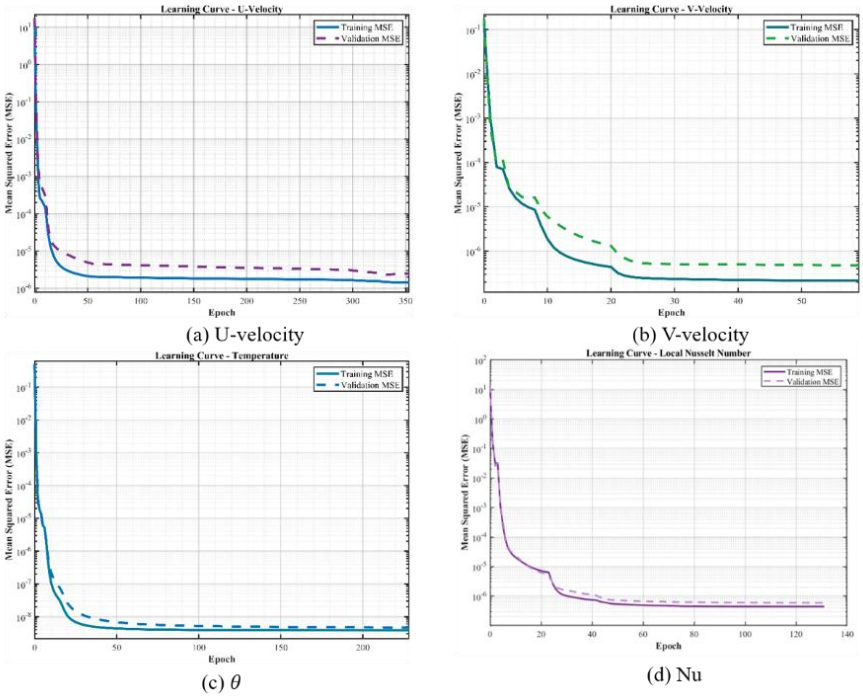


Figure 15. Training and validation MSE learning curves for (a) U, (b) V, (c) θ, and (d) Nusselt number.

The regression plots in Figure 16 demonstrate excellent agreement between the numerical targets and ANN predictions. The predicted points for the training, validation, testing, and complete datasets lie almost entirely along the ideal prediction line for all four quantities. The displayed R^2 values are essentially unity, accompanied by very small MSE values, confirming that the developed

networks accurately reproduce the numerical U-velocity, V-velocity, temperature, and Nusselt number data. The similarly strong performance across the training, validation, and testing subsets also indicates consistent predictive behavior rather than accuracy restricted to the training dataset.

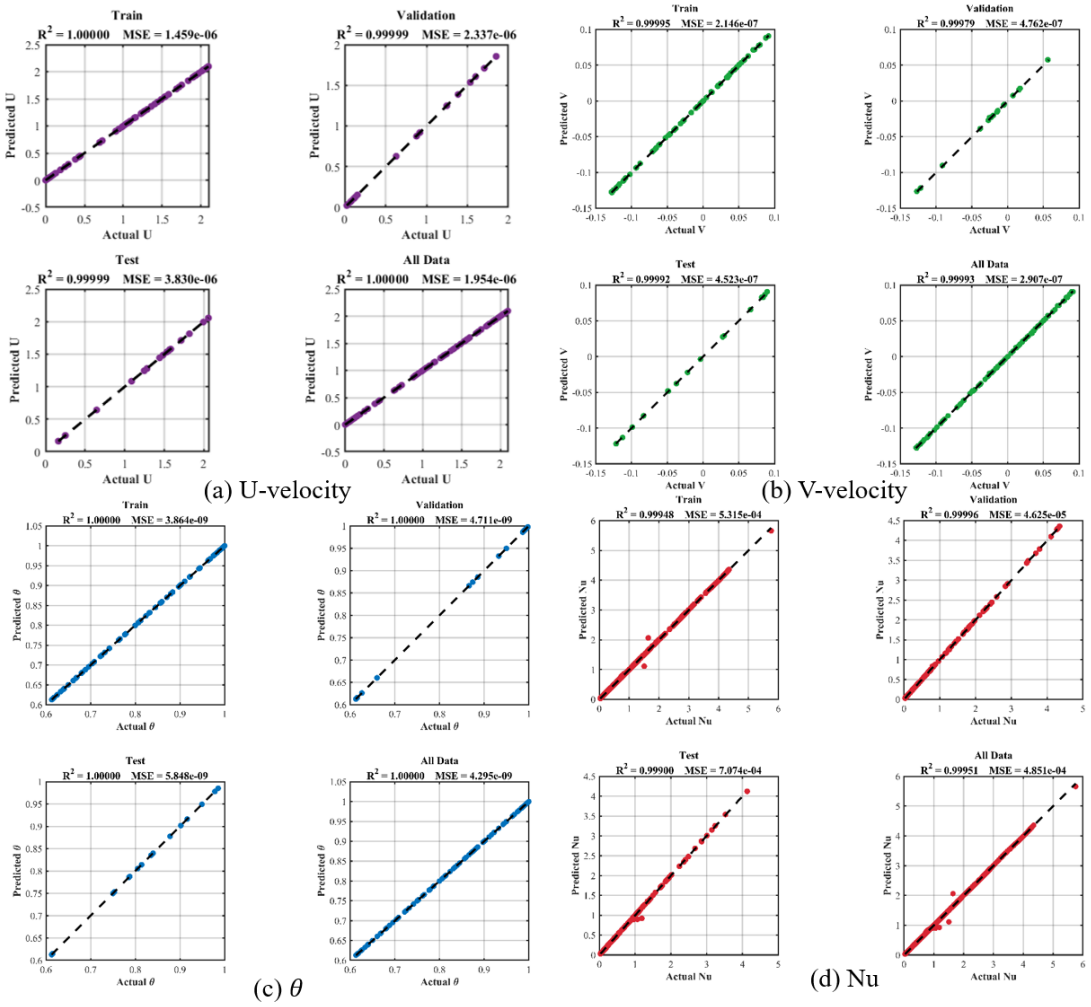


Figure 16. Regression analysis between numerical and ANN-predicted values for (a) U, (b) V, (c) θ and (d) Nusselt number.

Figure 17 shows the prediction error distribution for the four ANN outputs. In each case, the errors are strongly concentrated around zero, while their frequency decreases progressively toward the tails of the distributions. The narrow error ranges observed for the velocity and temperature predictions indicate a particularly small deviation between the ANN and the numerical results. Although the Nusselt number exabits a comparatively broader error range, its distribution also remains strongly centered near zero. These results indicate low systematic prediction bias and further support the accuracy of the developed ANN models.

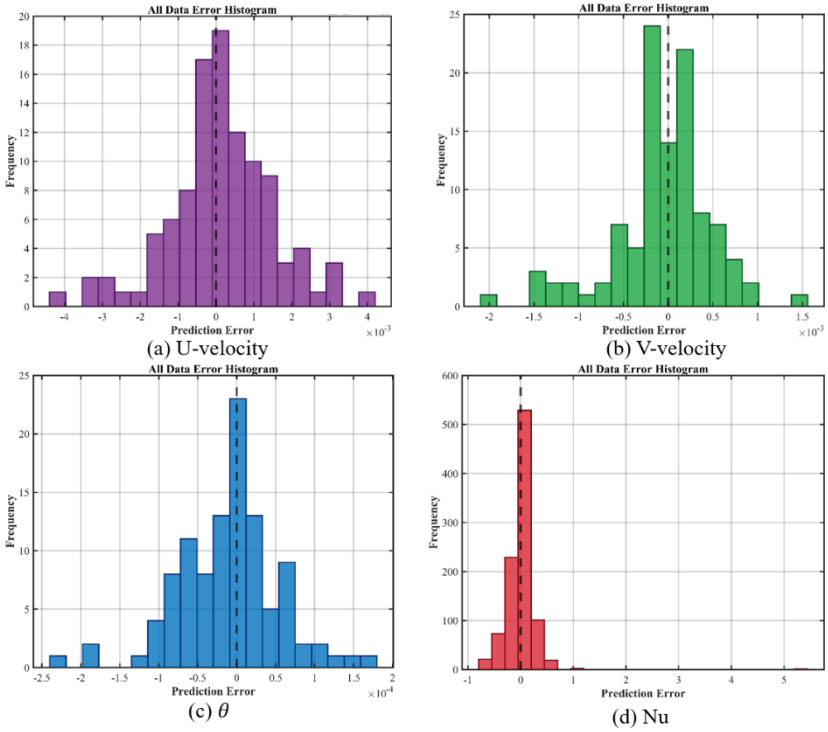


Figure 17. Prediction error histogram for (a) U, (b) V, (c) θ, and (d) Nusselt number (Nu).

Figure 18 compares the FEM results with the ANN-predicted values over the sample index for the U, V, θ, and Nusselt number. For all four quantities, the ANN predictions closely follow the corresponding FEM data, demonstrating the capability of the developed networks to reproduce the numerical response. Particularly strong agreement is observed for U-velocity, V-velocity, and temperature, where the ANN curves nearly overlap the FEM results despite the pronounced sample-to-sample variations. For the Nusselt number, the ANN also captures the overall variation and major peaks across the considerably larger dataset of 975 samples, although small deviations are observed at some sharp local extrema. These deviations can be attributed to the more nonlinear and rapidly varying behavior of the local heat transfer response. Overall, the close agreement between the FEM and ANN results confirms that the developed ANN models can effectively predict the principal flow and thermal characteristics of the system.

Figure 19 presents the probability density distributions of the ANN residuals. All four distributions exhibit pronounced peaks close to zero, demonstrating that most predictions differ only slightly from their corresponding numerical values. The relatively narrow distributions for U, V, and θ indicate particularly low prediction uncertainty, while the Nusselt number's distribution remains centered around zero despite its somewhat wider spread. The near-zero residual concentration is consistent with the regression and error histogram results and indicates the absence of substantial systematic over- or underprediction.

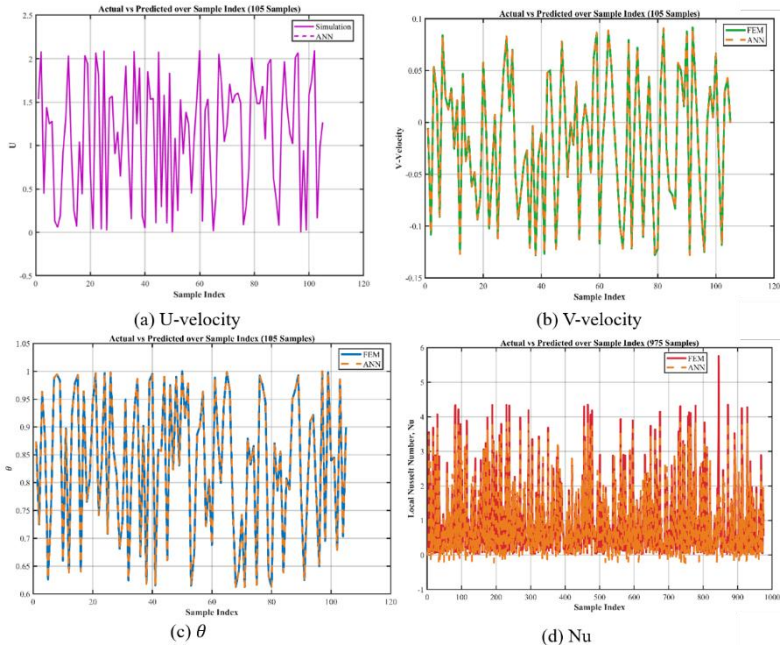


Figure 18. Actual and ANN predicted values over the sample index for (a) U, (b) V, (c) θ, and (d) Nusselt number (Nu).

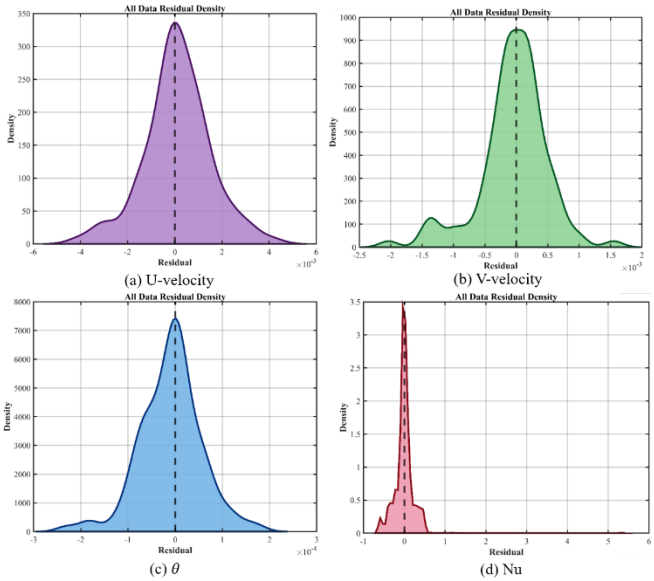
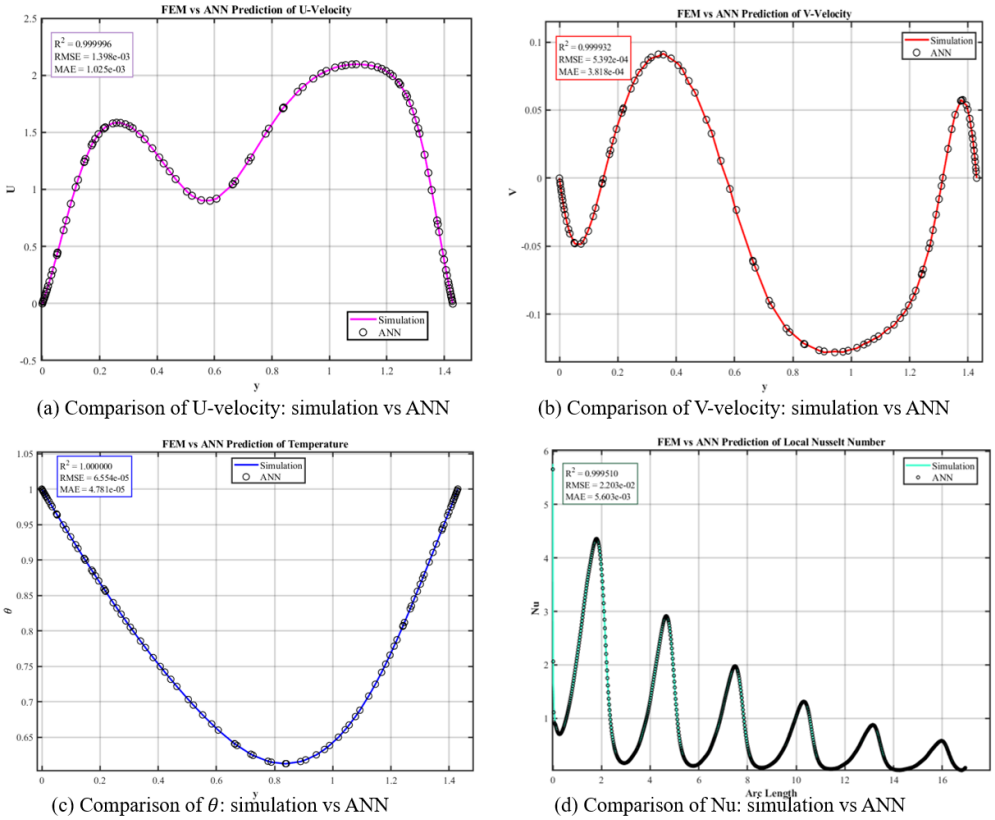


Figure 19. Residual probability density distribution for ANN-based predictions of (a) U, (b) V, (c) θ, and (d) Nusselt number (Nu).

Finally, Figure 20 directly compares the numerical profiles with the ANN's predictions for U-velocity, V-velocity, temperature, and the local Nusselt number. The ANN curves nearly coincide with the numerical profiles over the entire spatial domain, including the velocity maxima, the monotonic temperature variation, and the sharp peak in the local Nusselt numbers' distribution. In particular, the successful reproduction of the pronounced peak demonstrates that the ANN can capture not only smooth field variations but also relatively steep spatial gradients. The excellent

agreement between both approaches confirms the capability of the trained networks to accurately reproduce the numerical thermo-hydrodynamic responses.



(a) Comparison of U-velocity: simulation vs ANN

(b) Comparison of V-velocity: simulation vs ANN

(c) Comparison of θ: simulation vs ANN

(d) Comparison of Nu: simulation vs ANN

Figure 20. Comparison between the numerical simulation and ANN predictions for (a) U, (b) V, (c) θ and (d) Nusselt number (Nu).

6. Conclusions

The present study developed an integrated FEM-ANN framwork to investigate the thermo-hydraulic behavior of MHD forced convection of a Cu–CuO–Al_2O_3/water THNF in corrugated channels equipped with porous baffles. The principal originality of the work lies in the combined consideration of permeability-controlled porous baffles, corrugated isothermal walls, THNF transport, and magnetic damping within a unified thermo-hydraulic framework. Unlike conventional impermeable baffles, the porous configuration allows the fluid to penetrate through the obstacles, providing an additional mechanism for simultaneously controlling heat transfer enhancement and hydraulic resistance. The effect of the Re, Da, Ha, and particle volume fraction on the flow characteristics, heat transfer, and hydraulic performance were systematically analyzed. In addition, FEM-generated datasets were used to develop ANN surrogate models for reproducing the U-velocity, V-velocity, temperature, and local Nusselt number. The principal findings of this study are outlined below.

- Replacing conventional solid baffles with porous baffles improves the overall thermo-hydraulic performance by simultaneously enhancing heat transfer and reducing the pressure drop penalty. Compared with the solid baffle channel, the porous baffle channel

increased the average Nusselt number (Nu_{avg}) by approximetly 5.55% and reduced the pressure drop by 13.22% at Re = 250.

- Increasing the Re enhances convective heat transfer, resulting in a continous increase in the Nu_{avg} for both the solid and porous baffle channels. The porous baffle configuration consistently exhabits superioir thermal performance over the entire Re range.
- Increasing the Da increases the permeability of the porous baffle, allowing greater fluid penetration through the porous medium. Consequently, the Nu_{avg} increases by approximately 13.14%, while the pressure drop decreases by 9.36% as the Da increases from 10^{-6} to 10^{-2}.
- A stronger magnetic field suppresses the fluid's motion through the Lorentz force, which weakens convective heat transfer and increases hydraulic resistance. As a result, the Nu_{avg} decreases significantly, whereas the pressure drop increases with increasing Ha.
- Increasing ϕ improves the effective thermal conductivity of the THNF, leading to higher heat transfer rates. Despite the thermal enhancement, the greater effective viscosity of the suspension produces additional hydraulic resistance.
- The thermo-hydraulic performance index demonstrates that the porous baffle channel outperforms the conventional solid baffle channel over the investigated Re range (PI > 1). Moreover, the performance index increases with increasing Da, reaching its highest value at $\mathrm{Da} = 10^{-2}$ indicating that higher baffle permeability yields the optimum balance between convection-driven heat transfer and flow resistance.
- The developed ANN models successfully reproduce the FEM-computed U-velocity, V-velocity, temperature, and local Nusselt number. The close agreement between FEM and ANN predictions, together with the regression, MSE, prediction error, and residual analyses, demonstrate the capability of the data-driven models to capture the nonlinear thermo-hydrodynamic response of the system.

Overall, the results demonstrate that permeability-controlled porous baffles provide an effective strategy for improving the heat transfer–hydraulic resistance trade-off in corrugated channels. The integration of FEM with ANN further provides an efficient surrogate framework for representing the nonlinear thermo-hydrodynamic response within the investigated parameter ranges. These findings provide a basis for the design and optimization of compact thermal management systems involving porous flow control and magnetically influenced heat transfer. Future studies may extend the present framework to three-dimensional and transient configurations and experimentally validate the predicted thermo-hydraulic performance.

Author contributions

Talal Ali Alzahrani: Writing–review and editing, data curation, investigation, resources, funding, conceptualization, writing–original draft; Saleh Mousa Alzahrani: Formal analysis, visualization, investigation, project administration, methodology, writing–original draft, writing–review and editing. All authors have read and agreed to the published version of the manuscript.

Use of Generative-AI tools declaration

The authors declare they have not used artificial intelligence (AI) tools in the creation of this article.

Conflict of interest

The authors declare that they have no conflict of interest in this paper.

References

1. I. Pishkar, B. Ghasemi, Cooling enhancement of two fins in a horizontal channel by nanofluid mixed convection, *Int. J. Therm. Sci.*, **59** (2012), 141–151. https://doi.org/10.1016/j.ijthermalsci.2012.04.015
2. M. Khentoul, R. Bessaïh, Numerical study on entropy generation in a horizontal channel with fins using hybrid nanofluid, *Int. J. Heat Technol.*, **42** (2024), 501–510. https://doi.org/10.18280/ijht.420216
3. S. Y. Kim, J. W. Paek, B. H. Kang, Flow and heat transfer correlations for porous fin in a plate-fin heat exchanger, *J. Heat Transfer*, **122** (2000), 572–578. https://doi.org/10.1115/1.1287170
4. K. S. Arjun, K. Rakesh, Heat transfer by porous pin fins and nanofluid in rectangular minichannels, *Mechanika*, **24** (2018), 50–55. https://doi.org/10.5755/j01.mech.24.1.17284
5. T. Deshamukhya, D. Bhanja, S. Nath, Heat transfer enhancement through porous fins: A comprehensive review of recent developments and innovations, *Proc. Inst. Mech. Eng. Part C: J. Mech. Eng. Sci.*, **235** (2021), 946–960. https://doi.org/10.1177/0954406220939600
6. S. U. S. Choi, J. A. Eastman, Enhancing thermal conductivity of fluids with nanoparticles, In *Proceedings of the ASME 1995 International Mechanical Engineering Congress and Exposition*, San Francisco, CA, USA, 1995, 99–105. https://doi.org/10.1115/IMECE1995-0926
7. A. M. A. Smrity, P. Yin, Bridging computational and experimental boundaries: A review of theoretical modeling and experimental validation of hybrid nanofluids in heat transfer applications, *Int. J. Heat Fluid Flow*, **115** (2025), 109873. https://doi.org/10.1016/j.ijheatfluidflow.2025.109873
8. F. L. Rashid, N. M. L. Al Maimuri, K. A. Hammoodi, M. A. Eleiwi, I. Omle, A. M. M. Alsayyad, et al., Application of nanofluids for performance improvement of plate heat exchangers: A comprehensive review, *iScience*, **28** (2025), 113532. https://doi.org/10.1016/j.isci.2025.113532
9. F. L. Rashid, Z. A. K. Alkhekany, M. A. Eleiwi, A. Bouabidi, S. Ahmad, A. Chibani, et al., A comprehensive review on natural convection in trapezoidal cavities with mono and hybrid nanofluids, *Int. J. Thermofluids*, **27** (2025), 101226. https://doi.org/10.1016/j.ijft.2025.101226
10. A. Hafeez, D. Liu, A. Khalid, MHD flow of radiative hybrid nanofluid across a wedge influenced by melting heat transfer: Engineering application, *Alex. Eng. J.*, **122** (2025), 18–27. https://doi.org/10.1016/j.aej.2025.03.018
11. S. Khalid, M. Hussain, H. Waqas, D. Liu, Enhancing thermal energy storage efficiency with nano-integrated phase change materials: Machine learning-driven optimization via computational fluid dynamics, *Int. Commun. Heat Mass Transfer*, **167** (2025), 109221. https://doi.org/10.1016/j.icheatmasstransfer.2025.109221
12. B. Jalili, P. M. Zar, D. Liu, C. H. Ji, P. Jalili, M. A. H. Abdelmohimen, et al., Thermal study of MHD hybrid nano fluids confined between two parallel sheets: Shape factors analysis, *Case Stud. Therm. Eng.*, **63** (2024), 105229. https://doi.org/10.1016/j.csite.2024.105229

13. R. Mahmood, S. Bilal, A. H. Majeed, I. Khan, K. S. Nisar, CFD analysis for characterization of non-linear power law material in a channel driven cavity with a square cylinder by measuring variation in drag and lift forces, *J. Mater. Res. Technol.*, **9** (2020), 3838–3846. https://doi.org/10.1016/j.jmrt.2020.02.010
14. S. Bilal, M. Haseeb, N. Z. Khan, Thermal and mass diffusive mixed convective power law fluid flow in a lid-driven corrugated rectangular chamber with FEM simulations, *Therm. Adv.*, **8** (2026), 100173. https://doi.org/10.1016/j.thradv.2026.100173
15. H. Adun, D. Kavaz, M. Dagbasi, Review of ternary hybrid nanofluid: Synthesis, stability, thermophysical properties, heat transfer applications, and environmental effects, *J. Cleaner Prod.*, **328** (2021), 129525. https://doi.org/10.1016/j.jclepro.2021.129525
16. M. M. Alqarni, A. A. Memon, M. A. Memon, E. E. Mahmoud, A. Fenta, Numerical investigation of heat transfer and fluid flow characteristics of ternary nanofluids through convergent and divergent channels, *Nanoscale Adv.*, **5** (2023), 6897–6912. https://doi.org/10.1039/D3NA00818E
17. M. I. I. Rabby, M. W. Uddin, N. M. S. Hassan, M. Al Nur, R. Uddin, S. Istiaque, et al., Recent progresses in tri-hybrid nanofluids: A comprehensive review on preparation, stability, thermo-hydraulic properties, and applications, *J. Mol. Liq.*, **408** (2024), 125257. https://doi.org/10.1016/j.molliq.2024.125257
18. M. K. Nayak, A. A. Pasha, B. S. Kamilla, D. N. Thatoi, K. Juhany, M. Kouki, et al., Synthesis, stability, and heat transfer applications of ternary composite nanofluids—A review over the last decade, *Results Eng.*, **25** (2025), 104284. https://doi.org/10.1016/j.rineng.2025.104284.
19. A. Pandian, C. Boobalan, Ternary hybrid nanofluids: Synthesis, thermal properties, machine learning insights, and emerging applications, *Multiscale Multidiscip. Model. Exp. Des.*, **9** (2026), 6. https://doi.org/10.1007/s41939-025-01072-y
20. A. F. Khalaf, A. Basem, H. Q. Hussein, A. K. Jasim, K. A. Hammoodi, A. M. Al-Tajer, et al., Improvement of heat transfer by using porous media, nanofluid, and fins: A review, *Int. J. Heat Technol.*, **40** (2022), 497–521. https://doi.org/10.18280/ijht.400218
21. A. Jarray, Z. Mehrez, A. El Cafsi, Mixed convection Ag–MgO/water hybrid nanofluid flow in a porous horizontal channel, *Eur. Phys. J. Spec. Top.*, **228** (2019), 2677–2693. https://doi.org/10.1140/epjst/e2019-900068-8
22. A. I. Alsabery, A. S. Abosinee, New forced convection flow of nanofluid within a partially filled porous straight channel, *NJF Intell. Eng. J.*, **1** (2024), 77–88. https://doi.org/10.64179/3080-7549.1006
23. M. S. Rahomey, I. M. Abed, N. M. Said, Review of laminar forced convection in different shape channel with nanofluid superimposed in porous media, *Iraqi J. Mech. Mater. Eng.*, **24** (2025), 101–126. https://doi.org/10.32852/n34ncs25
24. G. B. Asbagh, S. Yarahmadi, M. Jafari, Heat transfer enhancement in multiphase systems: A systematic review of nanofluids, microchannels, and porous media, *Int. Commun. Heat Mass Transfer*, **170** (2026), 109998. https://doi.org/10.1016/j.icheatmasstransfer.2025.109998
25. Z. Min, S. Shaheen, M. B. Arain, A. Zeeshan, H. S. Hussein, AI-based analysis of heat transfer in Williamson nanofluids over a vertically stretching sheet, *Int. J. Hydrogen Energy*, **208** (2026), 153383. https://doi.org/10.1016/j.ijhydene.2026.153383

26. M. B. Arain, T. Mahmood, F. A. M. Al-Yarimi, M. A. Ali, S. Shaheen, J. Hu, On the study of acoustic-driven bubble dynamics in Williamson fluids with NARX neural networks, *Eng. Appl. Artif. Intell.*, **165** (2026), 113276. https://doi.org/10.1016/j.engappai.2025.113276
27. M. Zulfiqar, M. B. Arain, M. Zubair, Usman, H. Alhazmi, A numerical investigation of heat and mass transfer in the bioconvective Oldroyd B nanofluid flow through the porous stretching Riga surface with gyrotactic microorganism, *Case Stud. Therm. Eng.*, **72** (2025), 106431. https://doi.org/10.1016/j.csite.2025.106431
28. G. Sobamowo, Finite element thermal analysis of a moving porous fin with temperature-variant thermal conductivity and internal heat generation, *Rep. Mech. Eng.*, **1** (2020), 110–127. https://doi.org/10.31181/rme200101110s
29. S. E. Ahmed, Z. A. S. Raizah, M. A. Mansour, Z. Morsy, Impacts of multi-heat-generating porous fins on the flow structures and thermal fields of nanofluids within inclined U-shaped enclosures: Finite element method simulations, *J. Porous Media*, **25** (2022), 13–27. https://doi.org/10.1615/JPorMedia.2021039051
30. S. Rashidi, M. Bovand, I. Pop, M. S. Valipour, Numerical simulation of forced convective heat transfer past a square diamond-shaped porous cylinder, *Transp. Porous Media*, **102** (2014), 207–225. https://doi.org/10.1007/s11242-014-0272-0
31. K. H. Ko, N. K. Anand, Use of porous baffles to enhance heat transfer in a rectangular channel, *Int. J. Heat Mass Transfer*, **46** (2003), 4191–4199. https://doi.org/10.1016/S0017-9310(03)00251-5
32. N. B. Santos, M. J. S. de Lemos, Flow and heat transfer in a parallel-plate channel with porous and solid baffles, *Numer. Heat Transfer A*, **49** (2006), 471–494. https://doi.org/10.1080/10407780500325001
33. U. N. Hussein, N. S. Khashi'ie, N. M. Arifin, I. Pop, Heat transfer and flow dynamics of ternary hybrid nanofluid over a permeable disk under magnetic field and Joule heating effects, *Front. Heat Mass Transfer*, **23** (2025), 383–395. https://doi.org/10.32604/fhmt.2025.063023
34. R. Kundu, S. Islam, R. Aktary, S. Khatun, M. S. Islam, ANN and RSM-based comparison on a natural convective octagonal cavity containing ternary hybrid nanofluid including external magnetic field, *Eng. Rep.*, **7** (2025), e70348. https://doi.org/10.1002/eng2.70348
35. A. Haider, A. Ayub, Z. Yuan, Y. Nie, M. S. Anwar, T. Saidani, et al., Machine learning based modeling of pollutant and heat transfer in ternary nanofluid flow through porous media, *Chaos Soliton. Fract.*, **199** (2025), 116890. https://doi.org/10.1016/j.chaos.2025.116890
36. N. H. Hamza, F. Q. Al-Daamee, R. N. Kumar, R. Ghodhbani, F. Benabdallah, M. I. Khan, et al., Parametric study of magnetohydrodynamic-assisted heat transfer in nanofluid-filled corrugated channels with obstacles, *J. Inorg. Organomet. Polym. Mater.*, **35** (2025), 7565–7592. https://doi.org/10.1007/s10904-025-03748-x
37. S. Pati, A. Borah, M. P. Boruah, P. R. Randive, Critical review on local thermal equilibrium and local thermal non-equilibrium approaches for the analysis of forced convective flow through porous media, *Int. Commun. Heat Mass Transfer*, **132** (2022), 105889. https://doi.org/10.1016/j.icheatmasstransfer.2022.105889
38. V. Rajesh, M. Sheremet, Free convection in a square ternary hybrid nanoliquid chamber with linearly heating adjacent walls, *Nanomaterials*, **13** (2023), 2860. https://doi.org/10.3390/nano13212860

39. A. S. Mahdy, T. H. Al-Arabi, A. M. Rashad, W. Saad, MHD mixed convective heat transfer of Cu–Al_2O_3 water hybrid nanofluid over a stretching wedge with ohmic heating, *Int. J. Heat Technol.*, **40** (2022), 475–481. https://doi.org/10.18280/ijht.400215
40. P. Warrier, A. Teja, Effect of particle size on the thermal conductivity of nanofluids containing metallic nanoparticles, *Nanoscale Res. Lett.*, **6** (2011), 247. https://doi.org/10.1186/1556-276X-6-247
41. M. Turkyilmazoglu, Unsteady convection flow of some nanofluids past a moving vertical flat plate with heat transfer, *J. Heat Transfer*, **136** (2014), 031704. https://doi.org/10.1115/1.4025730



AIMS Press

© 2026 the Author(s), licensee AIMS Press. This is an open access article distributed under the terms of the Creative Commons Attribution License (https://creativecommons.org/licenses/by/4.0)